JOURNAL OF AIRCRAFT
Vol. 55, No. 3, May–June 2018

System-Level Assessment of Active Flow Control for Commercial Aircraft High-Lift Devices

Yu Cai,* Zhenyu Gao,* Imon Chakraborty,† Simon Briceno,‡ and Dimitri N. Mavris§
Georgia Institute of Technology, Atlanta, Georgia 30332

DOI: 10.2514/1.C034401

The use of active flow control technology for augmentation of aircraft aerodynamic performance is of considerable interest to the aerospace industry. Research to date has included subscale and full-scale wind-tunnel experiments as well as limited flight-test demonstrations. Out of several possible applications of active flow control to commercial aircraft, this paper focuses on its application to high-lift devices, which may permit weight and drag reduction through simplification of the flap mechanism. These, however, must be traded off against the additional weight of the active flow control system, its power requirements, and redundancy considerations to assess net system-level impacts. In this work, the Integrated Subsystem Sizing and Architecture Assessment Capability is used to assess the system-level impact of multiple high-lift device active flow control architectures for a small twin-aisle aircraft. A comparative assessment of these architectures reveals a strong dependency of fuel burn performance and the identity of the best-performing architecture on the system total mass flow requirements. For a selected architecture, the impact of the system mass flow requirements on the off-design performance is investigated. Despite an increase in vehicle operating empty weight, fuel consumption still decreases for most missions in the payload–range envelope. Finally, the sensitivity of the architecture's performance to several sources of uncertainty is ascertained through a sensitivity analysis, and it is observed that the uncertainty in estimation of flap track fairing drag has the most significant impact on the estimation of mission fuel burn.

I. Introduction

THE principle of active flow control (AFC) is to manipulate the high-receptivity regions of the flowfield around a vehicle with minimal energy input to attain advantageous flow conditions that in turn bring about improved vehicle performance [1]. Because of its perceived potential [2,3], significant AFC research has been and continues to be undertaken. This has included theoretical and experimental studies as well as flight tests for feasibility demonstration [4–12].

This paper focuses on one of many potential applications of AFC to a commercial transport aircraft: the augmentation of the aerodynamic performance of the high-lift devices (HLDs). The HLDs are used to enhance the lifting capability of the wings during low-speed (takeoff and landing) operations, permitting the aircraft to take off and land at acceptable airspeeds and within acceptable field lengths. HLD design over the past few decades has trended toward lighter and simpler single-slotted flaps as opposed to the earlier heavier and more complex double- and triple-slotted flap mechanisms [13]. Nevertheless, the HLDs continue to add considerable weight and maintenance burden to the aircraft. Further, to house the flap retraction/extension mechanisms, multiple fairings must be incorporated on the lower surface of the wing, which results in a drag penalty throughout the flight [5]. In this regard, the application of AFC to the HLDs may provide the following benefits:

1) The augmentation of aerodynamic performance may allow the same high-lift characteristics to be achieved with a simpler (e.g., simply hinged) flap mechanism, which is lighter.

2) The kinematics of the simpler mechanism may permit the elimination of the flap fairings, resulting in a reduction in aerodynamic drag.

Although these beneficial weight and aerodynamic impacts provide the incentive for high-lift device active flow control (HLDAFC) research, they are not sufficient to guarantee concept feasibility (i.e., whether the system can "buy its way onboard") because there are a number of additional technical challenges.

First, the incorporation of AFC system components will add weight to the aircraft. This includes not only the weight of the AFC actuators and pneumatic ducts but also the weight of additional power generation and distribution components required to supply the AFC system with the necessary secondary (nonpropulsive) power. Further, because catastrophic consequences may result from a sudden and precipitous loss of lift due to failure of the AFC system while in operation, it must necessarily be designed with suitable redundancy. As with other flight-critical systems, this requires the duplication of key system components, further adding to the weight penalty. Therefore, the reduction in aircraft operating empty weight (OEW) that was assumed in a prior study [5] may not necessarily materialize. Further, given the possibility of significant weight addition, a going-in assumption of weight neutrality (i.e., weight addition due to AFC would exactly neutralize weight reduction due to HLD simplification [14,15]) may also not be appropriate.

Second, for an AFC system sized to provide the requisite aerodynamic performance augmentation, the power requirements, though brief, may be of considerable magnitude. For the pneumatic sweeping-jet AFC actuators considered in this work, this means potentially large airflow requirements. The required aerodynamic performance augmentation is shown notionally in Fig. 1, for a landing approach scenario with approach velocity V_{app} that is 1.23 times the stall velocity V_{stall} of the conventional HLDs in landing configuration. For a given aircraft weight, this establishes the lift coefficient $C_{L,\text{app}}$ and angle of attack α_{app} of the nominal approach operating point $\boldsymbol{A}$ (Fig. 1). It should be noted that because $V_{\text{app}} = 1.23V_{\text{stall}}$, it follows that $C_{L,\text{app}} = C_{L,\max}/1.23^2 \approx 0.66C_{L,\max}$, and thus the nominal point $\boldsymbol{A}$ is in the linear portion of the lift curve [5]. The lower unaugmented (AFC off) aerodynamic performance of the simplified HLD at the same angle of attack (point $\boldsymbol{B}$) results in a lift deficit $\Delta C_L = \overline{\boldsymbol{BA}}$, which must be recovered through AFC-enabled lift augmentation to regain

Presented as Paper 2017-1627 at the AIAA SciTech Forum and Exposition, Grapevine, TX, 9–13 January 2017; received 27 January 2017; revision received 27 September 2017; accepted for publication 9 October 2017; published online 22 November 2017.

*Graduate Research Associate, Aerospace Systems Design Laboratory, School of Aerospace Engineering. Student Member AIAA.

†Research Engineer II, Aerospace Systems Design Laboratory, School of Aerospace Engineering. Member AIAA.

‡Senior Research Engineer, Aerospace Systems Design Laboratory, School of Aerospace Engineering. Senior Member AIAA.

§S.P. Langley Distinguished Regents Professor, Aerospace Systems Design Laboratory, School of Aerospace Engineering. Fellow AIAA.

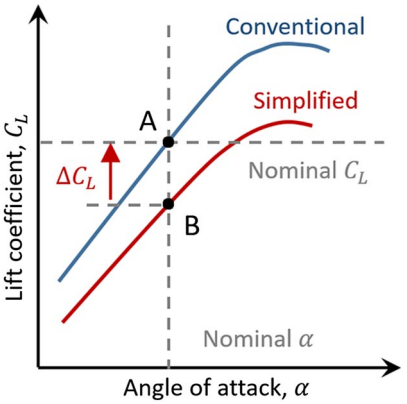

Fig. 1 Nominal lift condition for approach configuration with conventional and simplified flaps.

operating point ***A***. Although determination of the V_{app}/V_{stall} safety margin during AFC-enabled operation of the HLDAFC system is beyond the scope of this work, it is clear that the system power (flow) requirements depend on 1) the magnitude of the ΔC_L to be recovered through AFC operation (Fig. 1), and 2) the effectiveness of the AFC actuators (i.e., required flow rate per unit lift increment, which is an area of active AFC research [16]). A review of recent related work [5,14] shows that mass flow requirement predictions are sensitive to modeling assumptions, Reynolds number effects, actuator placement, and operating mode, among others. Thus, the mass flow requirements, which are shown subsequently to exert a strong influence on overall HLDAFC feasibility, are clearly subject to considerable epistemic uncertainty.

Third, multiple architectural possibilities exist with regard to the source and type of nonpropulsive power that is used to drive the HLDAFC system. Traditionally, bleed air extracted from either the main engines [5,14] or the auxiliary power unit (APU) [8,9] has been considered as the supply source for pneumatic AFC applications. However, large airflow requirements may exceed their maximum bleed extraction limits. Further, the industry trend toward the reduced use of bleed air for aircraft subsystems [17] warrants consideration of architectures that do not use bleed air exclusively. In addition, large airflow requirements may also necessitate the use of multiple sources of secondary power for the HLDAFC system. The presence of multiple secondary power sources and types results in a combinatorial space of possible HLDAFC architectures.

This paper presents a system-level assessment of HLDAFC concepts that addresses the preceding challenges through an approach that features the following defining characteristics:

1) The combinatorial architecture space is explored through a comparative assessment of multiple HLDAFC architectures that differ in the sources and types of secondary power used to drive the system. These include architectures that are powered by one, two, and three secondary power sources.

2) Given the epistemic uncertainty regarding the system mass flow requirements, the performance of each architecture is assessed over ranges of assumed system total mass flow rates, which are upper-bounded by the bleed air and shaft-power extraction limits of the engines and the APU.

3) No prior assumptions are made regarding the impact on aircraft OEW. For each architecture, the system mass flow requirements are linked to the sizing (and thus the weight estimates) of the major additional components. Redundancy considerations drive the duplication of several system components as well as the incorporation of dedicated components for operation in failure mode.

4) Focusing on a particular selected architecture, the impact of various epistemic, technological, and operational uncertainties on architecture performance is ascertained through a sensitivity analysis.

The remainder of this paper is organized as follows. Section II provides a summary overview of the Integrated Subsystem Sizing and Architecture Assessment Capability (ISSAAC) [18], which is used to integrate the sizing of the HLDAFC with that of the aircraft. Section III describes the small twin-aisle aircraft (STA) vehicle baseline and enumerates the HLDAFC architectures considered within the scope of this work. Section IV describes the modeling and sizing approach for the considered HLDAFC architectures. Section V compares the performance of the HLDAFC architectures relative to a baseline STA not equipped with high-lift AFC. Finally, Sec. VI concludes the paper and highlights avenues for future work.

II. Integrated Subsystem Sizing and Architecture Assessment Capability

In this work, the performance of HLDAFC architectures is assessed using the Integrated Subsystem Sizing and Architecture Assessment Capability (ISSAAC). The intent of ISSAAC, whose main modules are depicted in Fig. 2, is to explicitly link the sizing and analysis of the aircraft subsystems with traditional aircraft sizing, with a focus on novel subsystem architectures. The underlying methodology itself is not tool-specific and requires a set of tools that collectively possesses the following functionalities: 1) aircraft sizing and mission performance analysis capability, 2) propulsion cycle analysis capability, 3) subsystem sizing and analysis capability, and 4) analysis integration capability (for sequencing execution of functions 1–3, passing relevant information between modules, and checking for analysis convergence). Further, the same tool may be used to satisfy more than one of the preceding functions. Currently, MATLAB is used to perform functions 3 and 4, Flight Optimization System (FLOPS), a tool developed by NASA Langley Research Center [19], for function 1, and Numerical Propulsion System Simulation (NPSS) [20] for function 2. A more thorough description of the underlying ISSAAC approach is available in separate works [18,21,22], whereas this paper limits itself to a brief and contextually relevant description of the main ISSAAC modules:

1) Definition of design requirements: these include the mission performance requirements (such as the payload–range envelope), the point performance requirements, and the aircraft notional concept. This work considers a small, twin-aisle, aft-tailed, tube-and-wing, turbofan commercial transport design for assessing HLDAFC architectures.

2) Traditional aircraft and engine sizing: this module defines the aircraft in terms of a geometric scale (using, for instance, the wing planform area S_w), a propulsive scale (using the required sea-level static thrust T_{SL}), and key weights such as the takeoff gross weight W_{TO} and the empty weight W_e. The subsystem weight buildup relationships within FLOPS (and most other similar tools) are based on regressions of historical data and therefore apply to conventional subsystem architectures. Subsequent modules compute the weight changes and associated impacts of novel architectures.

3) Candidate subsystem architecture descriptor: this provides a qualitative description of the subsystem architecture to be evaluated in terms of the design solutions for each of the subsystems (e.g., in this work, what types of secondary power from which sources are used in a HLDAFC architecture). For an automated investigation of a large number of subsystem architectures, the descriptors are typically obtained from a matrix of alternatives, as shown in Fig. 2.

4) Subsystem architecture sizing and evaluation: this module performs the sizing of the major power consuming elements, power distribution elements, and power sources within the subsystem architecture (a generalized representation of which is shown in Fig. 3a). The outputs of this module are the difference in weight ΔW_{sub} of the considered architecture relative to a conventional one, and time histories of the architecture's shaft-power requirement $P_{spx}(t)$, bleed air requirement $\dot{m}_{bx}(t)$, and direct drag increment $\Delta C_D(t)$. The latter three potentially time-varying quantities are computed for each subsystem and for the architecture as a whole.

5) Design mission performance analysis: the purpose of this module is to evaluate the impact of the subsystem architecture on the design mission performance. In this context, the design mission may be defined as any payload–range combination for which the aircraft is at its maximum takeoff weight (MTOW). As shown in Fig. 3b, the impact occurs through weight, secondary power requirements, and drag increments. This information, generated through the execution of the

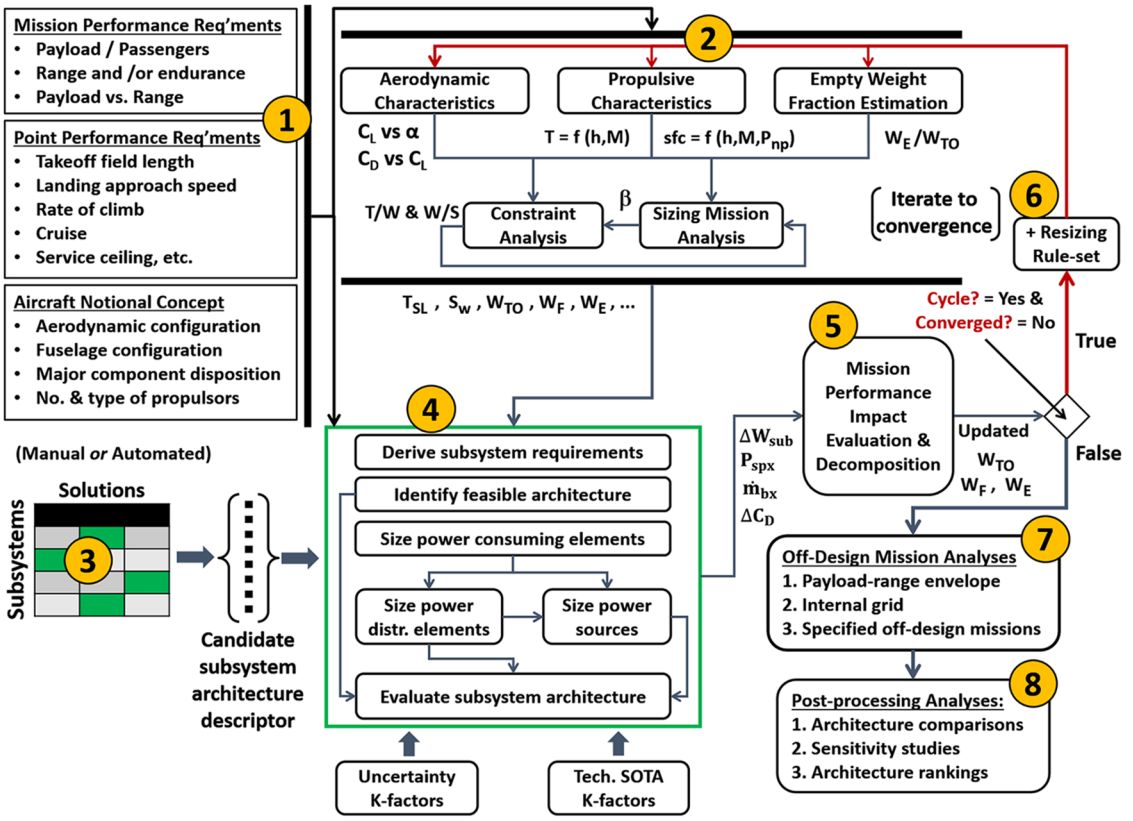

Fig. 2 Main modules of ISSAAC.

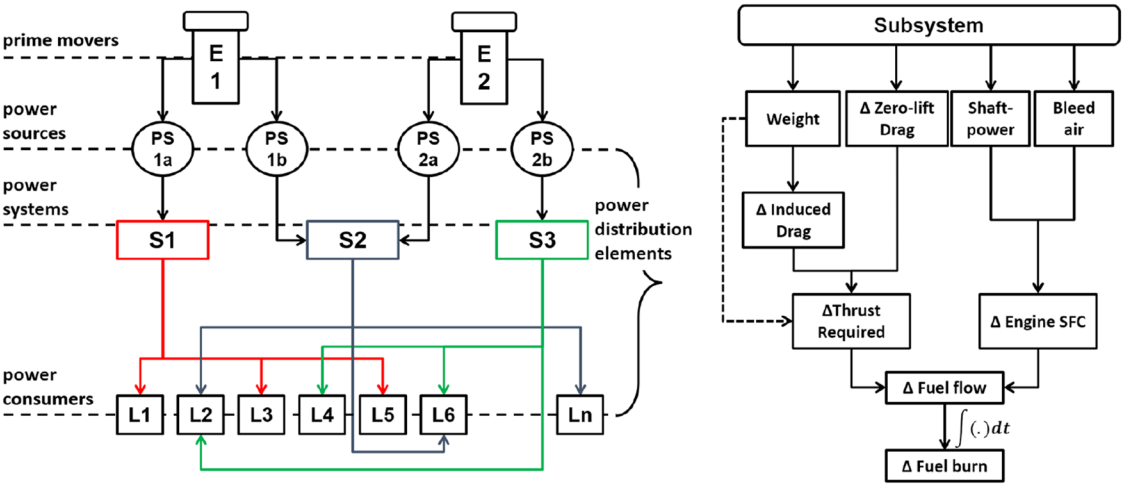

a) Generalized representation of elements and connectivity within an aircraft subsystem architecture

b) Impact of subsystems on fuel consumption (mission-level metric)

Fig. 3 Subsystem architecture and impact evaluation flow in ISSAAC.

previous module, is communicated to FLOPS through corresponding adjustment factors to reevaluate the design mission performance.

6) Resizing of aircraft and subsystems: this module governs an iterative resizing of the aircraft and its subsystems in accordance with certain resizing rules. For instance, the aircraft may be resized while maintaining a constant thrust-to-weight ratio and wing loading. The resizing of the aircraft is an optional step and is not performed within the scope of the current work.

7) Off-design mission performance analysis: following the evaluation of the performance of the aircraft for its design mission (and resizing, if chosen), the off-design mission performance is evaluated. This includes the determination of the payload–range envelope and the fuel consumption of off-design missions within the envelope.

8) Postprocessing analyses: this is a customizable module depending on the type of analysis being performed. For this work, the following are presented: a) performance assessment of multiple HLDAFC architectures over a range of system mass flow requirements (Sec. V.A), b) analysis of impact of a particular HLDAFC architecture on the aircraft's payload–range capabilities (Sec. V.B), and c) sensitivity analysis to determine impact of various sources of uncertainty on a particular architecture's predicted performance (Sec. V.C).

III. Baseline Aircraft and High-Lift Device Active Flow Control Architectures Considered

The impact of incorporating HLDAFC architectures is assessed with reference to a STA baseline, whose characteristics are

Table 1 Data summary for STA baseline without HLDAFC technology

Parameter	Value
Passenger capacity	242
Design payload weight	52,514 lb
Design range	7355 n mile
Harmonic range	5480 n mile
Ferry range	9648 n mile
Cruise Mach number	0.85
Maximum ramp weight	504,073 lb
Maximum payload weight	90,500 lb
Operating empty weight	264,852 lb
Maximum fuel capacity	223,378 lb
Sea-level static thrust	$2 \times 69,880$ lb
Wing planform area	4123 ft^2
Wingspan	198.9 ft
Wing aspect ratio	10.97
Wing taper ratio	0.159
Wing 1/4-chord sweep	32.1 deg
Wing dihedral	7.0 deg
Trailing-edge flaps stowed area	526 ft^2
Trailing-edge flaps span	111.8 ft
Trailing-edge flaps fairing	3 pairs
Horizontal tail planform area	822.7 ft^2
Horizontal tail aspect ratio	5.22
Horizontal tail taper ratio	0.243
Horizontal tail 1/4-chord sweep	36.6 deg
Vertical tail planform area	442.7 ft^2
Vertical tail aspect ratio	1.80
Vertical tail taper ratio	0.327
Vertical tail 1/4-chord sweep	40.6 deg

summarized in Table 1. For the analyses performed in this work, the aircraft is not resized (i.e., the maximum ramp weight and aircraft external geometry are held fixed). Further, the aircraft's maximum payload capacity is assumed to be held constant. Therefore, changes in aircraft empty weight on account of HLDAFC architectures result in a change in the fuel capacity and thus a shift in the right-hand boundary of the payload–range envelope. All the AFC architectures considered draw necessary power from the main engines and/or the APU. Assumptions and ground rules regarding the secondary (nonpropulsive) power capabilities of the engines and APU are established in Sec. III.A. The HLDAFC architectures that are analyzed within the scope of this work are then introduced and described in Sec. III.B.

A. Secondary Power Off-Take Limits

For both the main engines and the APU, there are limitations on the magnitude of bleed air and shaft-power that can be extracted. With regard to extracting secondary power from the main engines, the following assumptions and ground rules are enforced in this work:

1) Each baseline (mixed off-take) engine can supply 14.6 lb/s bleed air. This figure is obtained based on a) the maximum permissible bleed air extraction listed in the type certification data sheet of a representative engine as a percentage of core flow, and b) an estimate of the core flow for this thrust class of engine under landing approach conditions at flight idle power setting obtained from an NPSS engine model. The environmental control system minimum fresh airflow requirement for nominal operations [23], assessed at 0.55 lbm/ min per occupant for a total of 242 occupants, is assumed to be extracted equally from both engines. For simplicity, the same figure is assumed as a first estimate for the bleed air requirement of the ice protection systems [24]. The available bleed for HLDAFC is obtained by subtracting the requirements of these subsystems from the engine bleed capacity and is treated as a hard upper limit for all architectures using engine bleed air.

2) Each baseline (mixed off-take) engine is equipped with one 120 kVA electrical generator. The off-take to support cabin and avionics loads is estimated using data from published sources as 54 kVA per engine. However, it is assumed that the electrical generation capacity of each engine can be increased up to 500 kVA through the incorporation of two 250 kVA generators [17]. In this case, if the generator capacity per engine is $120 \leq P \leq 500$ kVA, then a generator mass increase (i.e., mass penalty) corresponding to the required up-sizing in power rating, $(P - 120)$ kVA, is assessed.

3) It is assumed that the main engines can simultaneously supply bleed air and electrical power within the aforementioned limits (in future work, this assumption will be tested by assessing engine operability and stability margins under such high mixed off-take conditions).

With regard to extracting power from the APU, the following assumptions and ground rules are enforced in this work:

1) The APU in the baseline aircraft is not used during flight. Therefore, the entire shaft-power or bleed capability of the APU is available for the HLDAFC system in the AFC-equipped aircraft if the APU is operated.

2) Any architecture making use of the APU may use either APU-supplied electricity or APU-supplied bleed air, but not both simultaneously.

3) The baseline (mixed off-take) APU is assumed to have 7.0 lb/s maximum bleed air supply capacity [9]. This is assumed to be a hard upper limit for all AFC architectures using APU bleed air.

4) The baseline (mixed off-take) APU is assumed to be equipped with a 120 kVA generator. However, it is assumed that the generation capacity of the AFC-equipped aircraft's APU can be increased up to 450 kVA through the incorporation of two 225 kVA generators [17]. If the APU power generation capacity of an architecture is $120 \leq P \leq 450$ kVA, then a generator mass increase (i.e., mass penalty) corresponding to the required up-sizing in power rating, $(P - 120)$ kVA, is assessed.

The ground rules listed previously for extraction of secondary power from the main engines and the APU impose different upper limits (constraints) for the maximum total airflow available for each AFC architecture considered. An unconstrained evaluation of the performance of each architecture is first obtained over a range of assumed total airflow requirements. Subsequently, the airflow and power constraints are imposed on this unconstrained solution space to obtain the constrained solution space.

B. High-Lift Device Active Flow Control Architectures Considered

This work considers only pneumatically powered sweeping jet actuators for the HLDAFC system. However, several system architecture possibilities exist with regard to the supply source(s) for the AFC actuators. The first and most obvious way to supply such actuators is to use bleed air, which may be extracted from the main engines, the APU, or both. However, the current industry trend is toward reduced bleed air off-takes from the engines and the elimination of bleed air off-take from the APU [17]. In light of this, another alternative is to compress externally admitted ram air using electrical compressors driven by electric power generated using shaft-power off-take from the engines and/or the APU. It should be noted that it may be necessary to use multiple supply sources (engines and APU) in case the AFC system airflow requirements are sufficiently large.

The presence of multiple secondary power sources (engines and/or APU) and secondary power types (shaft-power and/or bleed air) results in a combinatorial space of possible HLDAFC system architectures. The subspace considered in this work comprises 25 architectures that are summarized in Table 2. Bleed air may either not be used, or (if used) extracted from the main engines, APU, or both. Similarly, ram air may either not be used, or (if used) pressurized using compressors that obtain their electric power from the main engines, the APU, or both. For architectures in which both engine bleed air and ram air are used, five discrete ratios (from 1:9 to 9:1) are considered to cover the spectrum of possible distributions of the total mass flow requirement between the two. For architectures where the engines provide bleed air and the APU provides shaft-power, or vice versa, the loading priority determines which of the two resources is used preferentially. For instance, if engine bleed and APU shaft-power are considered and the engine is prioritized, then the entire bleed availability (for HLDAFC) of both engines has to be used before any APU shaft-power is used.

Table 2 Summary of HLDAFC architectures assessed

Architecture ID	Bleed air source	Electric power source	Engine bleed/ram air ratio	Loading priority	Test limits, lb/s Low	High
A-1	N/A	Engines	— —	— —	5	13
A-2	N/A	APU	— —	— —	5	7
A-3	N/A	Both	— —	— —	5	19
A-4	Engines	N/A	— —	— —	5	25
A-5	Engines	Engines	1: 9	— —	5	14
A-6	Engines	Engines	3: 7	— —	5	18
A-7	Engines	Engines	5: 5	— —	5	25
A-8	Engines	Engines	7: 3	— —	5	36
A-9	Engines	Engines	9: 1	— —	5	28
A-10	Engines	APU	— —	Engine	24	32
A-11	Engines	APU	— —	APU	5	32
A-12	Engines	Both	1: 9	— —	5	21
A-13	Engines	Both	3: 7	— —	5	27
A-14	Engines	Both	5: 5	— —	5	38
A-15	Engines	Both	7: 3	— —	5	36
A-16	Engines	Both	9: 1	— —	5	28
A-17	APU	N/A	— —	— —	5	7
A-18	APU	Engines	— —	Engine	5	20
A-19	APU	Engines	— —	APU	7	20
A-20	Both	N/A	— —	— —	7	33
A-21	Both	Engines	1: 9	— —	7	22
A-22	Both	Engines	3: 7	— —	7	25
A-23	Both	Engines	5: 5	— —	7	32
A-24	Both	Engines	7: 3	— —	7	43
A-25	Both	Engines	9: 1	— —	7	35

These rules are further explained through flowcharts (Figs. A1–A4) presented in Appendix A.

The test limits in Table 2 merely indicate the range of system total mass flow requirements over which the architectures are assessed. They are merely intended to envelope the actual air flow capabilities of each architecture. For most of the architectures, the lower testing limit is set to 5 lb/s. However, for architectures using APU bleed air and at least one other supply source, the lower limit is set to the APU maximum bleed capability of 7 lb/s. Evaluation of these architectures for mass flow rates less than 7 lb/s would not have required any additional supply source, resulting in those architectures essentially collapsing into A-17. A similar argument applies to the lower testing limit set for A-10. Within the set testing ranges, architectures are assessed over a 0.1 lb/s interval, which yields a total of 4805 architecture evaluations.

C. Redundancy Considerations

Other than some thrust interaction effects, the basic aerodynamic performance of conventional high-lift devices is not significantly affected by engine failure. However, because the HLDAFC system is directly powered by the engines and/or APU, failure of engines, APU, or pneumatic ducting could result in loss of mass flow supply and hence sudden loss of lift, potentially leading to the aircraft stalling. Therefore, redundancy of system components has been considered in laying out the HLDAFC architectures. Figure 4 shows schematically the general arrangement of components within the HLDAFC architectures considered in this work:

1) Air sources: bleed air may be extracted from the main engine cores and/or the APU. External ram air may also be admitted to serve as another air source.

2) Compressors: two compressors, left (Cmp-L) and right (Cmp-R), are considered. For architectures not using ram air, the compressors are used to charge the storage tanks using bleed air from the main engines or the APU. For architectures using ram air, the compressors pressurize the ram air to the necessary system supply pressure in supply mode and to the required storage tank pressure in charging mode. In this case, the compressors are sized based on the more demanding of the two modes. Each compressor has an associated motor drive and power control electronics and receives electrical power from generators driven by the main engines and/or the APU.

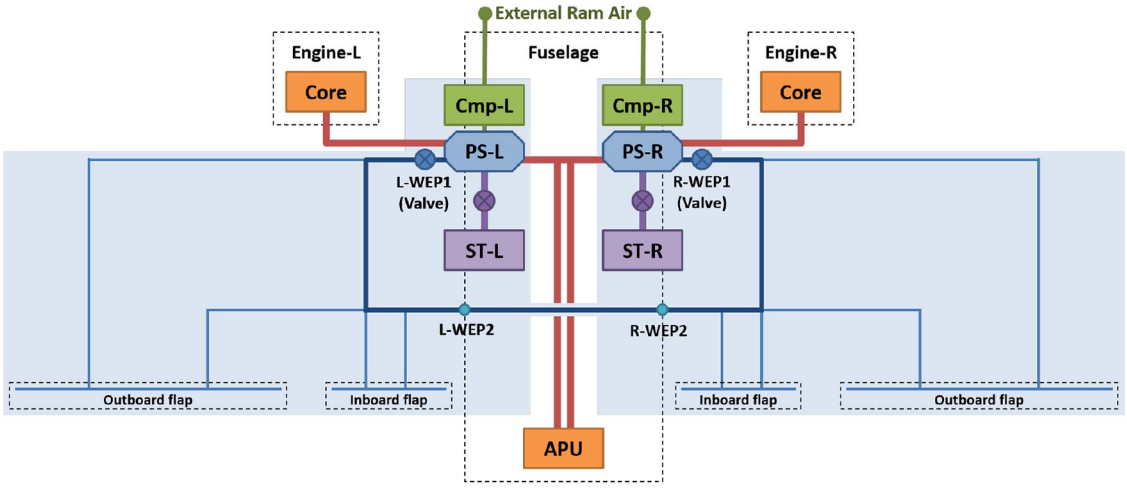

Fig. 4 HLDAFC architecture showing layout and connectivity of major components.

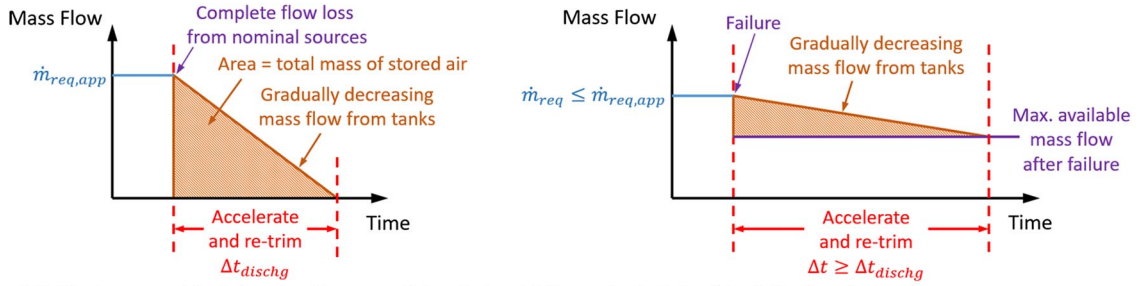

a) Critical case used to determine the mass of stored air b) General schedule of tank discharging

Fig. 5 Operation of storage tanks in emergency conditions.

3) Pneumatic systems: for redundancy, two pneumatic systems, left (PS-L) and right (PS-R), are considered. Under nominal operation, the left and right systems receive air supply from the port and starboard engines, respectively. Similarly, for architectures using ram air, the left and right systems receive compressed ram air from the left and right compressors, respectively. Both systems can receive APU bleed air. In case of failure of one system, cross-ducting allows the operating system to also supply the AFC actuators on the side of the failed system. In case of failure of one engine, the cross-ducting allows the other operating engine to supply the AFC actuators on the wing with the failed engine.

4) Storage tanks: all HLDAFC architectures, regardless of air supply source(s), are considered to have two storage tanks, left (ST-L) and right (ST-R), associated with the respective pneumatic systems. In charging mode, the storage tanks are pressurized using the compressor on the corresponding side, which in turn may pressurize external ram air, engine bleed air, or APU bleed air. As depicted in Fig. 5, in emergency discharge mode (following failure of one or more supply sources or supply lines), the storage tanks are designed to provide a gradually decreasing mass flow rate (that initially restores nominal flow rate and reduces gradually thereafter) over a specified interval of time, allowing the crew to react to the emergency and to retrim the aircraft to a higher airspeed. The storage tank discharge interval used for sizing pertains to complete loss of flow from nominal sources in the landing approach configuration, when flow requirements are the highest (Fig. 5a). For failures in the takeoff configuration or partial source failures, the flow requirement is lower, and thus the tanks can provide diminishing flow for a correspondingly larger duration (Fig. 5b).

5) Distribution ducting: engine core flow (if applicable) is assumed to reach the system through the existing bleed air ducting. An additional duct is added alongside the existing APU bleed air duct for redundancy. As mentioned previously, cross-ducting allows an operating system to supply the HLDs on the side of a failed system. Similar redundancy also exists in the peripheral ducting because the plenum of each flap panel is supplied by two supply ducts. The ducting is also geometrically separated through the use of multiple wing entry points for the left and right wings. Duct sizing is done based on the flow that would occur in off-nominal or failure conditions, which is no smaller than the flow rate under nominal operating conditions.

IV. Sizing and Analysis Approach for High-Lift Device Active Flow Control System

The following sections describe the sizing and analysis approach that is used for the HLDAFC system. This includes 1) the estimation of structural weight reduction (Sec. IV.A) and drag reduction (Sec. IV.B) due to flap mechanism simplification, 2) estimation of AFC actuator mass (Sec. IV.C) and distribution ducting mass (Sec. IV.D), 3) sizing of the storage tanks and the tank charging process (Sec. IV.E), 4) sizing of the electric compressors (Sec. IV.F), and 5) estimation of increased electric generator mass (Sec. IV.G). A consolidated summary of HLDAFC modeling parameters and relevant references is provided in Appendix B (Tables B1–B4).

A. High-Lift Device Structural Weight Reduction

The baseline non-AFC-equipped aircraft is assumed to have a single-slotted flap mechanism. The single-slotted flap mechanism kinematics of a modern small twin-aisle commercial aircraft [25] showed close agreement with the single-slot mechanism with link/track end support provided by Rudolph [13], who listed for it the following specific weights (weights per unit stowed flap area): flap panels, 2.7 lb/ft^2; supports, 1.5 lb/ft^2; actuation, 2.0 lb/ft^2; and fairing, 0.10 lb/ft^2. These total to a net specific weight of $w_{1\text{-slot}} = 6.3$ lb/ft^2.

For the AFC-equipped aircraft, the baseline single-slotted mechanism is assumed to be replaced by a simply hinged flap, maintaining the same flap dimensions and stowed area. The simply hinged flap weight is estimated using two different approaches. As per the first approach [26], the flap specific weight is estimated using the takeoff gross weight W_{to} as

$$w_{\text{simple}} = 2.089 k_{\text{tef}} \left(1 + \sqrt{\frac{W_{\text{to}}}{10^6}}\right) \text{[lb/ft}^2\text{]} \tag{1}$$

With a setting of $k_{\text{tef}} = 1$ for a trailing-edge flap system, this approach predicts a specific weight of $w_{\text{simple}} = 5.39$ lb/ft^2. However, one restriction of this method is that it is valid for $W_{\text{to}} < 200{,}000$ lb.

In a second approach, the specific weight of the simply hinged flap was estimated by removing the contribution of the fairings and 50% of the contribution of the support structures, while retaining the contributions from flap panels and actuation. This yields a simply hinged flap net specific weight of $w_{\text{simple}} = 5.4$ lb/ft^2, giving a flap specific weight change of $\Delta w_{\text{tef}} = -0.9$ lb/ft^2. The total flap weight change ΔW_{tef} is calculated by multiplying the stowed flap area S_{tef} by the change in flap specific weight between the two flap designs, Δw_{tef}:

$$\Delta W_{\text{tef}} = S_{\text{tef}} \cdot \Delta w_{\text{tef}} = S_{\text{tef}}(w_{\text{simple}} - w_{1\text{-slot}}) \tag{2}$$

With the baseline stowed flap area of 526 ft^2 and specific weights $w_{1\text{-slot}} = 6.3$ lb/ft^2, $w_{\text{simple}} = 5.4$ lb/ft^2, Eq. (2) predicts a 473 lb weight reduction due to simplification from a single-slotted flap to a simply hinged flap. This predicted weight reduction is applied to all architectures assessed in this work. It should be noted that, because the flap panel and support structures will have to sustain higher loading when the AFC system is activated, these elements may need to be reinforced. In the extreme case, the structural reinforcement may completely negate the advantage from simplifying flaps. The impact of such uncertainty in the predicted flap weight reduction is assessed through a sensitivity study (Sec. V.C.1).

B. Flap Fairing Drag Reduction

The use of simply hinged flaps makes possible the elimination of multiple flap fairings, which are used in conventional high-lift systems to house elements of the complex flap mechanism. The removal of external flap fairings results in a reduction in drag. The flap fairing drag contribution is proportional to the

maximum cross-sectional area of the fairing perpendicular to the airflow [27]. Hartwich et al. [14] cite a drag reduction of 1.65 counts per pair of external flap fairings, which are completely eliminated from a 275-passenger twin-aisle transonic commercial transport aircraft. Because of its geometric similarity with the STA baseline used in this work, this figure is used as the basis for computing the drag reduction through removal of external flap fairings. Under the assumption that the high-lift system has in total three pairs of flap fairings that can be removed, the corresponding drag reduction is 4.95 counts. The reduction in drag counts is applied to the drag coefficients seen over the course of the mission, which are then time-averaged to compute an overall percentage drag reduction for the aircraft, which is used in the mission performance analyses of the AFC-equipped architectures. Further, because a more detailed estimation of flap fairing drag reduction is not undertaken, the impact of uncertainty in this prediction is assessed through a sensitivity study (Sec. V.C).

C. Actuator and Control Valve Mass

AFC actuators and control valves are located along spanwise extent of the flaps. The total number of AFC actuators depends on the spacing between adjacent actuators. In this work, the total flap span of the STA baseline is 111.8 ft, and the nominal spanwise spacing is set to 0.75 ft, yielding a total of 148 actuator-and-control-valve combinations (ACVs). The weights of each AFC actuator and its associated control valve are estimated as 1.1 and 1.0 lb, respectively, based on Mooney et al. [9]. With these unit weights, the nominal ACV total weight is estimated to be $W_{\mathrm{ACV}} = 310.8$ lb. This estimate may change due to variations in spacing between adjacent actuators (thus, the total number of actuators) and variations in the unit weights of actuators and control valves. To study the impact of such weight variations on architecture performance, the ACV total weight is varied using a scaling factor K_{ACV} as part of a sensitivity analysis (Sec. V.C).

D. Additional Ducting Mass

The sizing of the distribution ducts focuses on three quantities: the inner diameter, the wall thickness, and the mass. The inner diameter of each segment D_i is determined using Eq. (3), derived from a relationship stated by Parrilla [28]:

$$D_i^{4.8} = 0.14211\left(\frac{RT_{\mathrm{nom}}}{p_{\mathrm{nom}}}\right)\mu^{0.2}\dot{m}^{1.8}\left(\frac{\Delta p}{L}\right)^{-1} \tag{3}$$

where R is the specific gas constant for air; T_{nom} is the nominal duct temperature; p_{nom} is the nominal duct pressure; μ is the air viscosity; $\dot{m}$ is the maximum mass flow rate in the duct segment determined during system sizing; Δp is the maximum permissible pressure loss between the pneumatic systems and the actuators; and L is the length of the longest duct from the AFC pneumatic systems to any actuator. The ducts are sized for the critical operating condition, where the mainline duct leaving one of the AFC pneumatic systems fails, and the other side has to supply the total mass flow required by HLDAFC system.

Grade 2 titanium [29] is used in AFC ducting. The duct wall thickness is computed based on the material properties and the burst pressure. The wall thickness of each duct segment is computed as shown in Eq. (4) [29]:

$$t_{w,\mathrm{duct}} = \frac{p_b D_i}{2\sigma_{\mathrm{eff}}} \quad \text{with} \quad \sigma_{\mathrm{eff}} = \sigma_{\max} - p_b(1 - Y) \tag{4}$$

where the burst pressure p_b is the product of the nominal pressure p_{nom} and the burst pressure factor; σ_{eff} is the effective material stress; $\sigma_{\max}$ is the maximum permissible stress; and Y is a factor for nonferrous metals. With the inner diameter, wall thickness, and length of each segment of duct, the duct mass can then be determined. Figure 6 shows the parametric definition of major HLDAFC system components within the aircraft's three-dimensional geometric model, from which lengths of duct segments are automatically computed by the ISSAAC HLDAFC evaluation script.

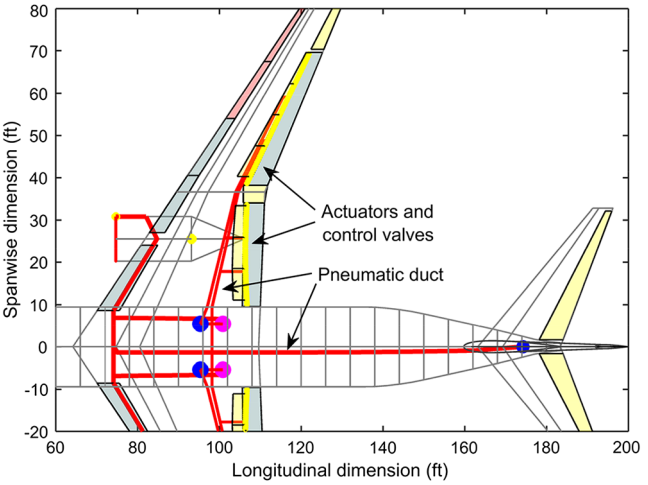

Fig. 6 Top-view showing major HLDAFC components within aircraft three-dimensional geometric model.

E. Storage Tank Sizing

A summary of the analysis procedure for storage tank charging is shown in Fig. 7. The tank dimensions (internal volume V_{tank} and external surface area A_{tank}) are fixed based on available space within the fuselage to house them. Before initiation of charging, the air in the tank is assumed to be at a minimum pressure $p_{\min}$ that is sufficiently higher than plenum pressure to guarantee positive airflow from the tank to the plenum. The initial temperature is assumed to be equal to the cargo bay temperature T_{bay}. The mass of air initially inside the tank is then given by $M_{\mathrm{air},i} = p_{\min}V_{\mathrm{tank}}/RT_{\mathrm{bay}}$. The supply air temperature T_{sup} and pressure p_{sup} depend on whether engine/APU bleed air or postdiffusion external ram air is being used. A convective heat loss $\dot{Q}_{\mathrm{conv}}$ is assumed due to temperature difference between the tank outer surface temperature (assumed to be $\approx T_{\mathrm{tank}}$) and bay temperature T_{bay}. To evaluate $\dot{Q}_{\mathrm{conv}}$, a convective heat transfer coefficient of $h_0 = 5\ \mathrm{W \cdot m^{-2} \cdot K^{-1}}$ is assumed to represent still air convection.

The requirement that the tank must be able to discharge an average mass flow rate $\bar{\dot{m}}_{\mathrm{dischg}}$ over a discharge interval $\Delta t_{\mathrm{dischg}}$ yields the mass of air that must be pumped into the tank during the charging process: $\Delta M_{\mathrm{air}} = \bar{\dot{m}}_{\mathrm{dischg}}\Delta t_{\mathrm{dischg}}$. When charging is complete, the final mass of air in the tank is given by

$$M_{\mathrm{air},f} = M_{\mathrm{air},i} + \Delta M_{\mathrm{air}} = \frac{p_{\min}V_{\mathrm{tank}}}{RT_{\mathrm{bay}}} + \bar{\dot{m}}_{\mathrm{dischg}}\Delta t_{\mathrm{dischg}} \tag{5}$$

A fixed efficiency η_{cmp} is assumed for the compressor. The pressure ratio Π across the compressor is the ratio of the tank pressure p_{tank} and the supply pressure p_{sup}. The instantaneous mass flow rate through the compressor $\dot{m}_{\mathrm{air}}$ depends on its rated power P_{cmp} and instantaneous pressure ratio Π. At low pressure ratios, $\dot{m}_{\mathrm{air}}$ may also be constrained by the available supply air flow.

As indicated in Fig. 7, the process equations for compression allow the evaluation of the instantaneous compressor exit temperature T_{cet} and power requirement P_{req}. The ideal gas relationship along with mass and energy conservation equations allow the evolution of tank air mass M_{air}, pressure p_{tank}, and temperature T_{tank} to be tracked.

A cylindrical geometry with spherical end caps is assumed for the storage tanks, with a diameter of 5 ft and total length of 13 ft. The tanks are sized based on the final pressure $p_{\mathrm{tank},f}$ indicated by the

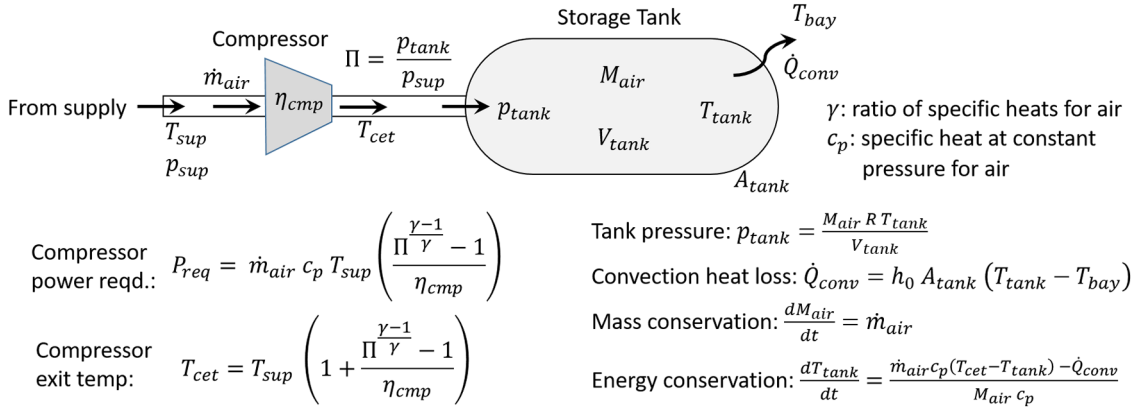

Fig. 7 Summary of main relationships for storage tank charging process.

charging process. The pressure difference across the tank walls is computed as $\Delta p_{\text{tank}} = p_{\text{tank},f} - p_{\text{bay}}$, where p_{bay} is the pressure of air in the bay where the tanks are housed. Wall thickness of the cylindrical tank is calculated based on circumferential (Hoop) stress considerations as

$$t_{w,\text{tank}} = \frac{\Delta p_{\text{tank}} D_{\text{tank}}}{2\sigma_y \lambda} \cdot f_s \tag{6}$$

where D_{tank} is the tank diameter, σ_y is the yield strength of the wall material, $f_s = 1.4$ is an engineering factor of safety, and $\lambda < 1$ is a factor accounting for reduction in material strength at elevated temperatures. These factors as well as material density were obtained under the assumption that the tanks are constructed of maraging steel [30]. The mass of the sized tanks is then estimated based on basic geometric relationships and material density.

F. Compression System Sizing

In all architectures considered, electric compressors are used to charge the storage tanks. To determine the required compressor power rating in charging mode, the charging process (Fig. 7) is simulated with an assumed compressor power rating P_{cmp} to check whether it is sufficient to pump the required air mass ΔM_{air} into the storage tank within the stipulated charging time Δt_{chg}. The power rating P_{cmp} is then updated iteratively to find the minimum compressor power rating $P_{\text{cmp,chg}}$ that satisfies this charging criterion.

Additionally, for architectures that use external ram air as one of the air sources for the HLDAFC system, the compressors serve the additional function of pressurizing the admitted air to the required supply pressure p_{sup} in supply mode. In this case, the power required by the compressor is given by

$$P_{\text{cmp,sup}} = \dot{m}_{ra} C_p T_{\text{cmp,in}} \left(\frac{\Pi^{(\gamma-1)/\gamma} - 1}{\eta_{\text{cmp}}}\right) \tag{7}$$

where $\dot{m}_{ra}$ is the mass flow rate of ram air handled by the compressors, for which an overall efficiency η_{cmp} is assumed. The pressure ratio across the compressor is given by $\Pi = p_{\text{sup}}/p_{\text{cmp,in}}$, where $p_{\text{cmp,in}}$ is the total pressure of air entering the compressor. The total temperature and pressure of air entering the compressor ($T_{\text{cmp,in}}, p_{\text{cmp,in}}$) are obtained from relationships for diffusion through ram air inlet diffusers:

$$T_{\text{cmp,in}} = T_\infty \left(1 + \frac{\gamma - 1}{2} M_\infty^2\right) \tag{8}$$

$$p_{\text{cmp,in}} = \eta_{\text{rd}} p_\infty \left(1 + \frac{\gamma - 1}{2} M_\infty^2\right)^{\gamma/(\gamma-1)} \tag{9}$$

where η_{rd} is the efficiency of the ram air diffuser. The freestream temperature, pressure, and Mach number ($T_\infty, p_\infty, M_\infty$) were computed for a 140 kt sea-level approach condition.

The compressor required power rating is then given by the maximum of the power required in charging and supply modes: $P_{\text{cmp}} = \max(P_{\text{cmp,chg}}, P_{\text{cmp,sup}})$. With this power rating, the compressor mass M_{cmp}, the electric drive motor mass M_{em}, and the power electronics mass M_{pe} are added to obtain the total mass of the compression system, M_{CS}:

$$M_{\text{cmp}} = \frac{P_{\text{cmp}}}{(P/M)_{\text{cmp}}} \tag{10}$$

$$M_{\text{em}} = \frac{P_{\text{cmp}}}{(P/M)_{\text{em}}} \tag{11}$$

$$M_{\text{pe}} = \frac{P_{\text{cmp}}}{(P/M)_{\text{pe}} \eta_{\text{em}} \eta_{\text{pe}}} \tag{12}$$

$$M_{\text{CS}} = M_{\text{cmp}} + M_{\text{em}} + M_{\text{pe}} \tag{13}$$

In Eqs. (10–12), $(P/M)_{\text{cmp}}$, $(P/M)_{\text{em}}$, and $(P/M)_{\text{pe}}$ are power-to-mass ratios (PMR) of the compressor, electric drive motor, and power electronics, respectively. Motor and power electronics efficiencies are respectively η_{em} and η_{pe}. The effect of uncertainty in the three preceding PMR is subsequently assessed through a sensitivity analysis (Sec. V.C).

G. Additional Generator Mass

As described previously, the required power rating of the HLDAFC system compressors is determined as the maximum of that required for 1) tank charging requirements, and 2) system supply (if applicable). The efficiency of the electric motors, power electronics, and distribution network are then taken into account to determine the net generator power output required to satisfy these requirements. Based on the available (unused) power capacity of the main engine and/or APU generators (as the case may be), the required up-sizing or increase of electrical generation capacity $\Delta P_{\text{gen,inc}}$ is computed. The corresponding increase in electrical generator mass is computed using the power-to-mass ratio of electrical generators $(P/M)_{\text{gen}}$ as

$$\Delta M_{\text{gen}} = \frac{\Delta P_{\text{gen,inc}}}{(P/M)_{\text{gen}}} \tag{14}$$

The effect of varying the generator power-to-mass ratio $(P/M)_{\text{gen}}$ is ascertained subsequently through sensitivity analyses in Sec. V.C.

H. Net Weight Impact of High-Lift Device Active Flow Control System

The net impact on vehicle OEW W_e due to installing the HLDAFC system consists of two parts.

1) Weight addition brought by HLDAFC system components, including the actuators, control valves, ducts, compression system, pneumatic system, and storage tanks:

$$W_{\mathrm{AFC}} = (W_{\mathrm{ACV}} + W_{\mathrm{duct}} + W_{\mathrm{CS}} + W_{\mathrm{PS}} + W_{\mathrm{ST}}) \times (1 + K_{\mathrm{misc}}) \quad (15)$$

where a miscellaneous weight factor K_{misc} with a nominal value of 0.15 serves to account for weight of installation and insulation, which is an uncertainty factor to be assessed in sensitivity analysis (Sec. V.C).

2) Change in weight of existing components, including weight reduction of trailing-edge flaps, $\Delta W_{\mathrm{tef}} < 0$, and weight penalty due to generator up-sizing (if required), $\Delta W_{\mathrm{gen}} \geq 0$.

To summarize, the net impact on W_e is calculated as follows:

$$\Delta W_e = W_{\mathrm{AFC}} + \Delta W_{\mathrm{tef}} + \Delta W_{\mathrm{gen}} \quad (16)$$

V. Performance and Sensitivity Assessment of High-Lift Device Active Flow Control Architectures

The following sections describe the evaluation of the HLDAFC architectures of Table 2 using the described approach. Section V.A shows the fuel burn performance of all the considered architectures over a range of assumed system mass flow requirements. Section V.B then shows the variation in the payload–range capabilities of a single architecture due to the incorporation of HLDAFC. Finally, Sec. V.C shows the impact of various sources of uncertainty on the performance of this same architecture.

A. Evaluation of High-Lift Device Active Flow Control Architecture Space

Each architecture's performance is first assessed over the range of mass flow rates shown in Table 2. Subsequently, infeasible architecture/mass flow combinations, which violated the main engine and/or APU secondary power off-take limits (constraints) established in Sec. III.A, are filtered out. The performance curves of each of the considered HLDAFC architectures over the feasible range of mass flow requirements are shown in Fig. 8. In each subplot, the required mass flow rate is plotted on the x axis. The y axis shows the fuel burn performance expressed as a percentage-delta (%-Δ) relative to a non-AFC-equipped baseline. The correct way to interpret a point (x, y) from the curve for Architecture "k" is as follows.

For Architecture k, assuming that the AFC system's effectiveness/efficiency permits the necessary ΔC_L to be recovered with x lb/s of total mass flow rate, the resulting impact on fuel burn relative to a non-AFC baseline is y %.

Figures 8a–8f are described as follows.

1) Figure 8a shows the performance of all 25 architectures over their respective ranges of feasible mass flow rates. For each architecture, as the mass flow rate requirement increases, the mass additions to the airplane to support the AFC architecture also increase, progressively negating the fuel savings made possible by the fairing drag reduction and flap mechanism weight reduction.

2) Figure 8b shows the performance of five architectures in which the AFC power requirements are met through both engine shaft-power extraction (SPX) and bleed air extraction (BX), in different combinations. The ratios in the legend indicate the manner in which the total required mass flow is split between engine bleed air and external ram air (which is compressed using electrically driven compressors, thus consuming shaft-power). For instance, "1:9" implies that 10% of the total mass flow requirement is obtained from main engine bleed air, whereas the remaining 90% is admitted as ram air and compressed using electric compressors. With the main engine secondary power extraction limits established as ground rules, it is seen that A-8, with a 7:3 split between engine bleed air and external ram air, can supply the highest mass flow rate. The magnitude of the degradation in fuel savings with increasing mass flow rate (due to additional system hardware) increases with the proportion of ram air usage. This is due to significant mass additions due to electric compressors, drive motors, and motor power control electronics required to compress the ram air to the necessary supply pressure.

3) Figure 8c shows architectures that require only a single form of secondary power (shaft-power or bleed air), which is obtained either from the main engines or the APU, or both. Among these, the maximum feasible mass flow rate is for A-20, which uses bleed air from the main engines and the APU simultaneously.

4) Figure 8d shows five architectures in which a certain fraction of the net mass flow requirement is directly obtained as engine bleed air. To provide the electrical power to compress the remaining fraction (which is obtained as ram air), the existing APU generator capacity is first used. If this is insufficient, then the available excess capacity of the main engine generators is used. If still insufficient, APU generator up-sizing is resorted to, up to a maximum of 450 kVA. If still insufficient, main engine generators can be up-sized to a limit of 500 kVA per engine. It is seen that A-14, with a 50/50 split between engine bleed air and ram air, has the highest airflow capacity of all architectures within this subplot.

5) Figure 8e shows architectures that use both forms of secondary power, deriving different forms from the engines and the APU. For each architecture in this subplot, the secondary power source which is listed first is first used completely. If shaft-power (electricity) is used first, then the loading sequence "use existing generator capacity → use existing bleed capacity → up-size generator capacity" is followed. If bleed air is used first, then the corresponding loading sequence is "use existing bleed capacity → use existing generator capacity → up-size generator capacity".

6) Figure 8f shows five architectures that use APU bleed air and a combination of engine shaft-power and bleed. The APU bleed capability is first used fully. The remaining portion of the mass flow requirement is then split between main engine bleed and external ram air as per the given ratio (as described previously). It is seen that A-24, which uses APU bleed followed by a 7:3 split of the remaining requirement between main engine bleed and ram air (compressed by main engine shaft-power), can support the highest mass flow rate of all architectures considered.

It is also observed that, when the engines supply both bleed air and shaft-power (Figs 8b, 8d, and 8f), at a certain system mass flow requirement, reducing the use of ram air improves fuel saving. However, intermediate mass flow ratios generally have the highest mass flow capacity.

Because all the architectures enjoy the same weight and drag reduction due to simplification of the HLDs, the differences in the fuel burn performance are largely driven by the differences in HLDAFC architecture mass. Therefore, the trends seen in Fig. 8 are also seen if %-Δ OEW is plotted instead of block fuel (Fig. C1, Appendix C).

Figure 9 shows how the identity and the fuel savings of the best-performing architectures (based on magnitude of fuel savings over the reference mission) varies with the assumed total mass flow requirement. Generally, at higher mass flow requirement, more complex and heavier architectures are required, which partially negate the fuel savings. Because A-24 has the highest feasible maximum airflow capacity and range of feasible airflows of all architectures considered within the scope of this paper, the off-design performance and sensitivity analyses in the following sections are performed for this architecture.

B. Effect on Payload Range

The off-design mission performance of A-24 is assessed for system mass flow requirements of 10, 20, 30, and 40 lb/s. The resulting payload–range charts are shown in Figs. 10a–10d. The dotted line shows the payload–range boundary for the non-AFC-equipped

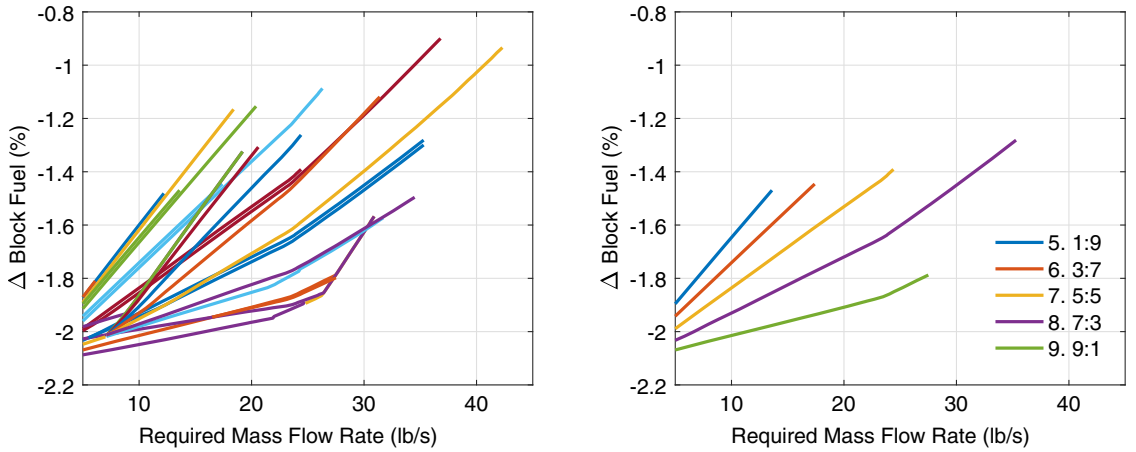

a) All architectures

b) A-5 – A-9: engine BX & SPX

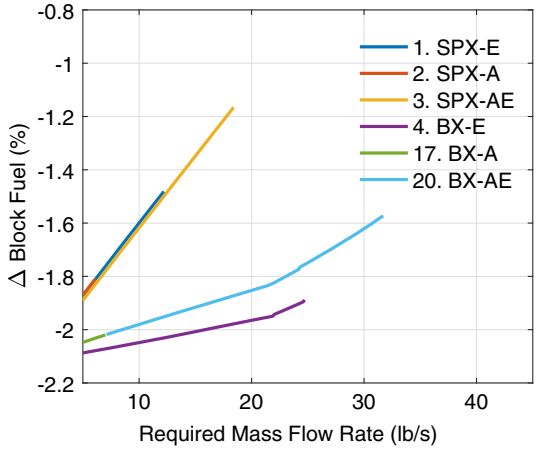

c) Architectures using SPX or BX exclusively

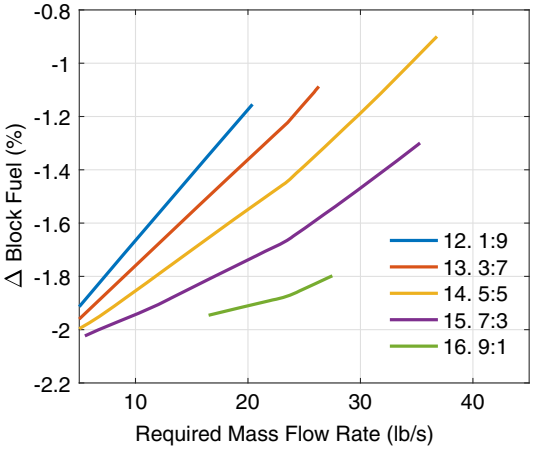

d) A-12 – A-16: engine BX & SPX + APU SPX

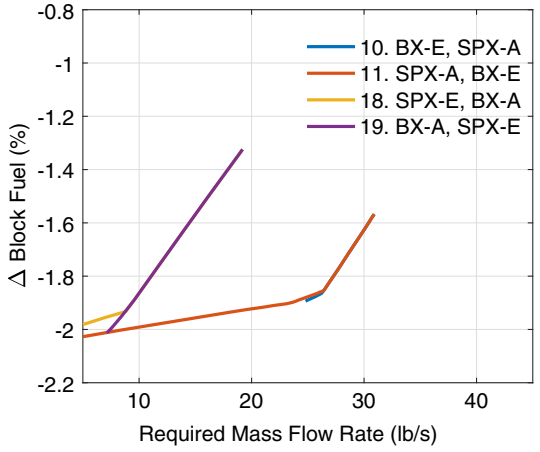

e) A-10, A-11, A-18, and A-19

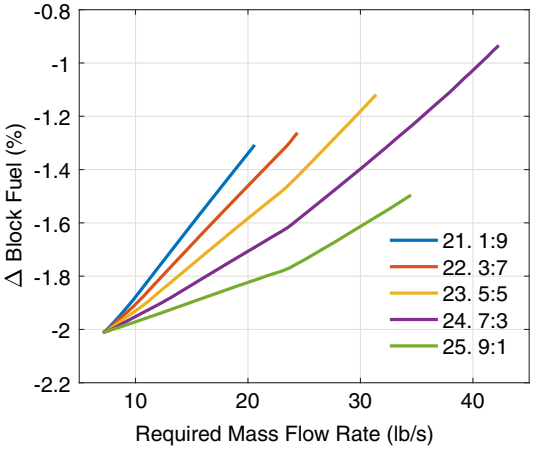

f) A-21 – A-25: engine BX & SPX + APU BX

Fig. 8 Impact of mass flow requirements on fuel burn of considered HLDAFC architectures.

baseline, whereas the solid line shows the boundary for A-24 for the assumed flow rates.

For points on the longer of the sloped boundaries of the payload–range chart, the aircraft is at its MTOW (which is identical for both A-24 and the non-AFC-equipped baseline). Because the OEW increases due to incorporation of the HLDAFC system, the AFC-equipped aircraft can carry less fuel than the non-AFC-equipped baseline for the same payload. At the same time, the AFC-equipped airplane benefits from drag reduction due to elimination of flap fairings. The net impact on harmonic range (maximum range with full payload) of these two counteracting effects is determined by the system mass flow requirement. This is shown in Table 3. If the mass flow requirements are low, then the drag benefit overcomes the weight penalty, resulting in a gain in harmonic range. However, if the required mass flow is higher, then this trend is quickly reversed. A similar trend is also seen for the maximum range at design payload. The subplots of Fig. 10 show a corresponding leftward shift on the right-hand boundary with increasing mass flow requirements.

Though not of particular economic value, it is interesting to note that the AFC-equipped aircraft always sees an increase in ferry range capability. Under these conditions, the airplane has no

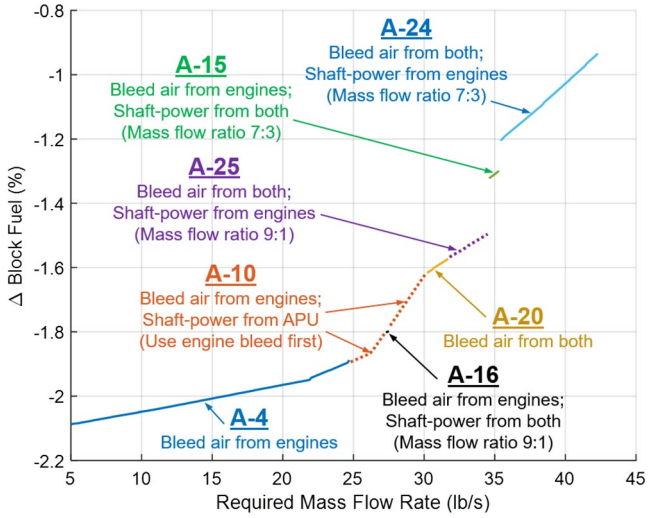

Fig. 9 Fuel burn benefits for best-performing architectures vs mass flow requirement.

payload, it is at maximum fuel capacity (identical for both AFC-equipped and non-AFC-equipped aircraft), and the takeoff gross weight of the aircraft is well below MTOW. Under these conditions, the elimination of fairing drag provides a fuel burn advantage for the AFC-equipped aircraft.

Table 3 also shows the fuel burn reduction of A-24 over the reference mission for each assumed mass flow requirement. Fuel burn performance at other off-design conditions is indicated by the shading within the payload–range charts. These comparisons are only valid for payload–range combinations that can be flown by both AFC-equipped and non-AFC-equipped aircraft. Simultaneous inspection of the shading within all the subplots reveals how the average fuel burn saving reduces significantly with assumed system mass flow requirements. Inspection of individual subplots shows that, for a given assumed mass flow requirement, the fuel burn savings are higher for longer range missions. For very short-range missions, the AFC-equipped aircraft can actually be at a fuel burn disadvantage relative to the non-AFC-equipped baseline. For such missions, the fuel penalty to overcome the added aircraft weight especially during climb outweighs the fuel savings through drag reduction for the significantly shorter cruise segment.

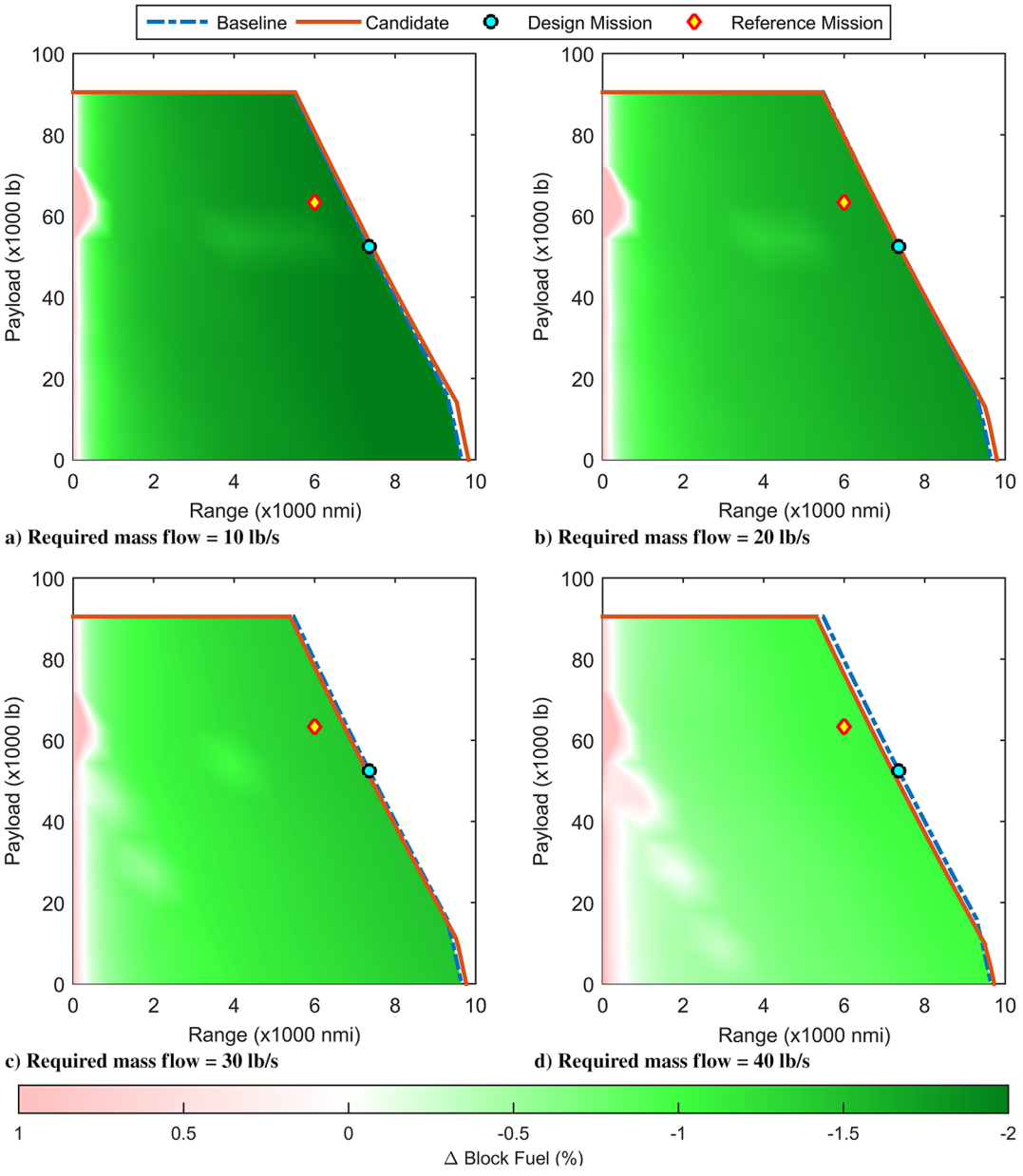

Fig. 10 Effect of HLDAFC on payload–range performance of A-24.

Table 3 Effect of HLDAFC system mass flow requirements on key performance metrics of A-24

A-24 performance Δs (relative to non-AFC baseline)	HLDAFC system mass flow requirement, lb/s			
	10	20	30	40
Δ operating empty weight, %	+0.65	+1.09	+1.65	+2.31
Δ block fuel for reference mission (6000 n mile, 63,350 lb payload), %	−1.95	−1.71	−1.40	−1.03
Δ harmonic range (max 90,500 lb payload), n mile	+38 (+0.70%)	−18 (−0.33%)	−89 (−1.62%)	−173 (−3.16%)
Δ range at design payload (52,514 lb payload), n mile	+72 (+0.97%)	+11 (+0.15%)	−65 (−0.88%)	−156 (−2.12%)
Δ ferry range (zero payload), n mile	+175 (+1.81%)	+150 (+1.55%)	+118 (+1.22%)	+80 (+0.83%)

Table 4 Summary of K-factors for uncertainty analysis

Parameter	Low	Nominal	High
Epistemic uncertainty K-Factors			
Change in flap specific weight Δw_{tef}, lb/ft^2	−1.08	−0.9	0.18
Reduced fairing drag coefficient ΔC_{Df}, count	3.96	4.95	5.94
ACV total weight scaling factor K_{ACV}	0.7	1.0	1.3
Miscellaneous weight factor K_{misc}	0.1	0.15	0.2
Technology SOTA K-Factors			
Generator PMR $(P/M)_{gen}$, kW/kg	2	2.76	5
Power electronic PMR $(P/M)_{pe}$, kW/kg	2	2	6
Electric motor PMR $(P/M)_{em}$, kW/kg	2	4	8
Compressor PMR $(P/M)_{cmp}$, kW/kg	2	2.5	3
Operational Uncertainty K-Factors			
Tank charging time t_{chg}, s	300	600	900
Tank discharging time t_{dischg}, s	10	20	30
Required plenum pressure p_{req}, atm	1.5	2.5	3

C. Sensitivity to Epistemic, Technological, and Operational Uncertainties

The sensitivity analyses presented in the following sections pertain to the performance of architecture A-24 over a reference mission (63,350 lb payload over a 6000 n mile range). As shown in Table 4, a total of 11 K-factors are chosen to represent (through their variation) the effect of epistemic uncertainty, technological state-of-the-art (SOTA), and uncertainty in operational parameters. The uncertainty analyses are conducted for mass flow rates of 10, 20, 30, and 40 lb/s. For each mass flow rate, a 4000-point Latin hypercube design of experiments in the K-factors was prepared to evaluate the performance of A-24 with each combination of K-factor settings.

Multivariate regression was performed using the statistical analysis tool JMP to generate the prediction profiler plots shown in Figs. 11–13. In each of these figures, the rows correspond to the tested mass flow rates of 10, 20, 30, and 40 lb/s. Columns correspond to the K-factors that were varied during the sensitivity analysis. The *y* axis intervals are identical for all rows, subplots, and figures, and thus the magnitude of a K-factor's influence is indicated by the slope of the sensitivity curves and by the height of the sensitivity indicator triangles (which indicate the magnitude of the partial derivative of the response with respect to the K-factor evaluated at the K-factor setting). The vertical crosshairs indicate the nominal setting of the corresponding K-factor. The horizontal crosshairs indicate the resulting %-Δ block fuel for the nominal K-factor setting.

1. *Sensitivity to Epistemic Uncertainty*

The impact of the epistemic uncertainty K-factors on the block fuel performance of A-24 is shown in Fig. 11. The impact of uncertainty regarding drag reduction due to elimination of flap

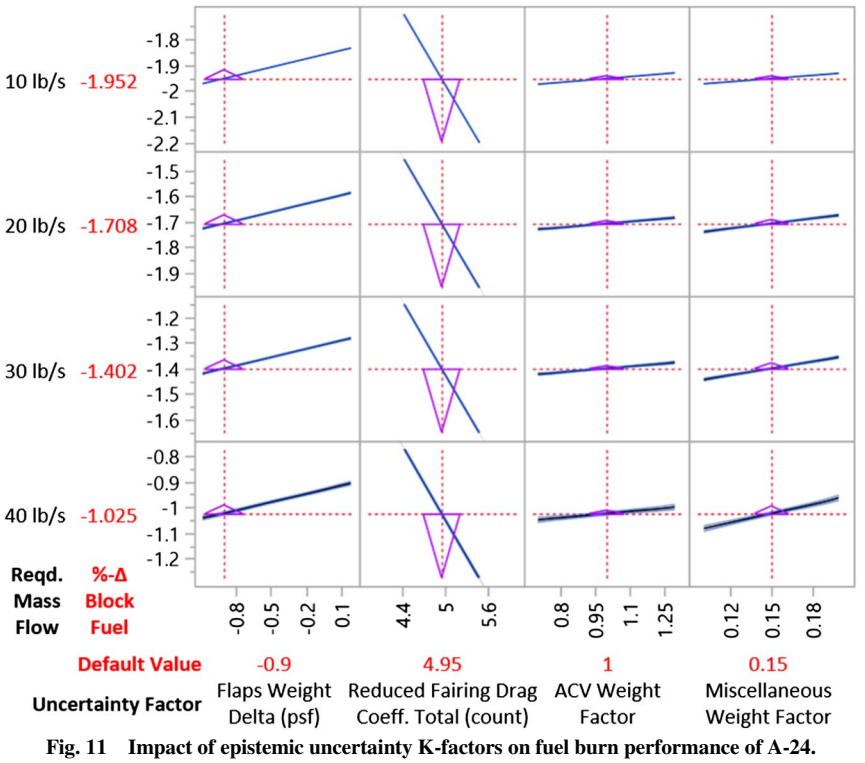

Fig. 11 Impact of epistemic uncertainty K-factors on fuel burn performance of A-24.

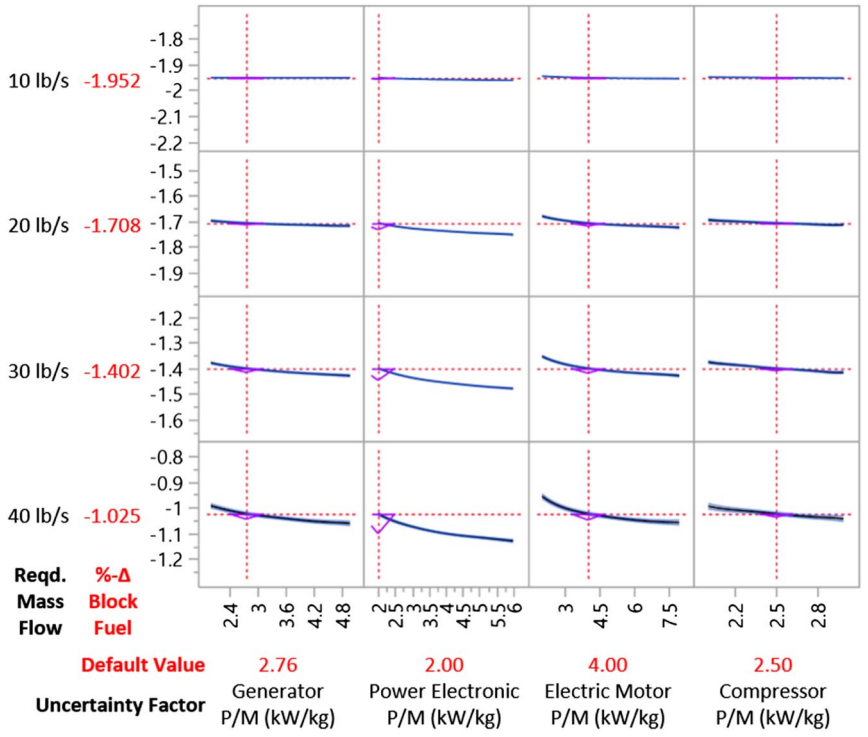

Fig. 12 Impact of technology SOTA K-factors on fuel burn performance of A-24.

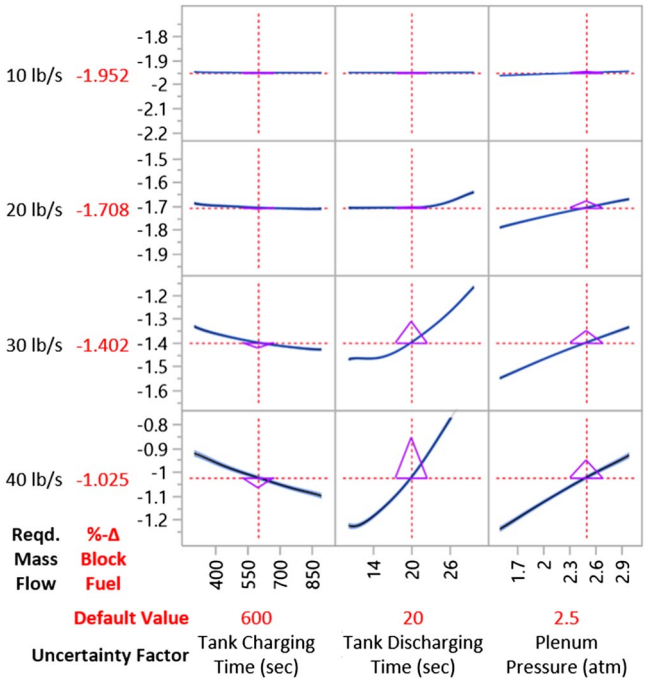

Fig. 13 Impact of operational K-factors on fuel burn performance of A-24.

fairings is seen to have a significant influence. This is much larger than the impact of uncertainty in flap weight reduction (Δw_{tef}) and uncertainty regarding weights of actuators and control valves (W_{ACV}, influenced by K-factor K_{ACV}). These three sensitivities do not vary with variation in the system total mass flow rate requirement.

The change in flap specific weight w_{tef} is varied between -1.08 and $+0.18$ lb/ft^2, or $[-20, +120\%]$ of the nominal value. This range of values accounts for cases where the reinforcement of flap mechanism (to sustain higher AFC-induced air loads) partially or even fully negates the weight benefit from simplification of flap mechanism, as mentioned in Sec. IV.A. Compared to the nominal case, the estimated fuel saving for the reference mission would be reduced by approximately 0.1% if the change of flap mechanism is weight neutral, regardless of the system mass flow requirement.

The influence of the factor K_{misc}, however, does increase with increasing mass flow rates. This is due to the fact that the miscellaneous mass is computed as a fraction of the masses of certain explicitly sized components, which increase with increase in mass flow rate. Overall, this factor has a greater influence than Δw_{tef} and K_{ACV}.

In summary, the influence of uncertainty in the predicted drag reduction (ΔC_{Df}) is much more significant than those related to weights (Δw_{tef}, K_{ACV}, and K_{misc}). Therefore, to reduce the impact of epistemic uncertainty, it would be prudent to invest more effort in obtaining a better estimate of the drag contribution from the fairings and thus the drag reduction due to their elimination.

2. *Sensitivity to Technological State-of-the-Art*

The impact of technological SOTA on the performance of A-24 is shown in Fig. 12. Higher values of these power-to-mass ratios represent improving technology, which means lower masses for the corresponding components when sized to the same rated power. Therefore, the mass addition to the aircraft is lower, and the corresponding fuel burn performance improves (i.e., a lower, more negative %-Δ block fuel).

The effect of power-to-mass ratio of electric generators $(P/M)_{\text{gen}}$ is not as significant if the mass flow requirement is low because either generators may not need to be up-sized or the magnitude of the up-sizing may be small. The influence of power-to-mass ratio of power electronics $(P/M)_{\text{pe}}$ is somewhat larger and becomes more significant with increasing mass flow requirement because a larger magnitude of electrical power must be handled. The same general trends are seen for the power-to-mass ratios of electric motors $(P/M)_{\text{em}}$ and compressors $(P/M)_{\text{cmp}}$. The gradually flattening slopes of the curves for higher values of the K-factors indicate the onset of diminishing returns (i.e., for higher power-to-mass ratios,

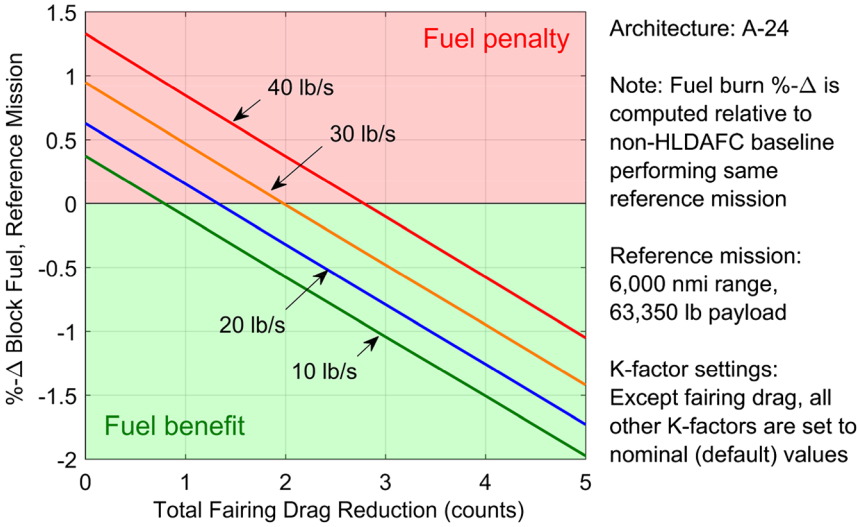

Fig. 14 Impact of total fairing drag reduction on fuel burn performance of A-24.

the component mass for a given power rating is lower, and less is gained by further improvement of the power-to-mass ratio thereafter).

3. *Sensitivity to Operational Parameters*

The sensitivities of the block fuel performance of A-24 to variations in operational parameters such as tank charging time, tank discharging time, and plenum pressure are shown in Fig. 13. It is evident from the slopes of these curves that the influence is quite substantial.

The tank charging time does not have a significant influence for low mass flow rates because the ratings (thus, masses) of compressors, motors, and power electronics are then determined by the supply mode rather than the charging mode. The influence becomes more significant with increasing mass flow requirements, as the charging mode begins to drive compressor sizing. For a given mass flow requirement, relaxing the charging time constraint reduces the power rating (and thus mass) of the compression system, resulting in improved fuel burn benefits.

The tank discharging time also does not have a significant influence for low mass flow rates. However, for higher mass flow rates, the impact is seen to be much more pronounced. An increase in the required discharge time increases the mass of air that must be held in the storage tanks, thereby increasing the tank pressurization requirements and the associated power (and mass) of the compression system.

The impact of the HLDAFC system's plenum pressure increases with mass flow requirement and affects both the supply and charging modes of the compression system. The supply mode is affected because the compression system must pressurize the admitted ram air to a higher discharge pressure. The charging mode is affected because the higher plenum pressure necessitates an even higher minimum pressure of the storage tanks (to ensure positive airflow), which drives up the necessary compression power.

4. *Sensitivity to System Mass Flow Requirement and Fairing Drag Reduction*

The preceding sensitivity study reveals that the uncertainty in system mass flow requirement and flap fairing drag reduction have the most significant impact on fuel burn performance. The analyses up to this point are based on the assumption that the fairings are completely eliminated, as proposed by Hartwich et al. [14], which is the most optimistic scenario. Because of the observed high sensitivity to the fairing drag reduction, the predicted fuel saving will suffer if 1) the fairings cannot be completely eliminated, or 2) the predicted drag reduction was overly optimistic. Such scenarios are assessed by varying the reduction in fairing drag coefficient over an even wider range, between zero (i.e., fairing drag remains unchanged) and five drag counts. The resulting impact of varying only mass flow requirement and fairing drag reduction (with all other K-factors at default values) on fuel burn is presented in Fig. 14. Generally, as the system mass flow requirement increases, the reduction in fairing drag necessary to achieve a certain fuel saving increases. For instance, if the mass flow requirement is 10 lb/s, a reduction of 0.8 drag count (16% of the nominal value) is sufficient for A-24 to gain fuel benefit over the reference mission. However, if the mass flow requirement is 40 lb/s, the fairing drag reduction must reach at least 2.8 drag counts (57% of the nominal value) to see a fuel benefit. It should be noted that a combination of low baseline fairing drag (thus low drag reduction potential) and high mass flow requirement will make it more difficult to extract a meaningful fuel burn benefit.

VI. Conclusions

This work presented a system-level assessment of multiple high-lift device active flow control architectures, using the Integrated Subsystem Sizing and Architecture Assessment Capability to link the sizing of the active flow control system to the mission performance analysis of a small twin-aisle aircraft. The analysis revealed that the system total mass flow requirement had a significant influence on both the magnitude of the performance improvement and on the identity of the best-performing architecture. When the assumed mass flow rate requirement was swept within the interval 5 to 43 lb/s, the corresponding fuel burn savings for the best-performing architectures varied between 2.09 and 0.92%. The mass flow rate was seen to have a similarly prominent influence on the off-design mission performance for a selected active flow control architecture. The mass flow requirement affected the operating empty weight, the boundary of the payload–range envelope, and the fuel burn impact of the aircraft when operating within the new envelope. For mass flow requirements in the range of 10–40 lb/s, the corresponding operating empty weight increments ranged from +0.65 to +2.31%. The fuel burn benefit ranged from 1.95 to 1.03%. At the highest mass flow rate of 40 lb/s, the reduction in range at design payload was 156 n mile. A sensitivity study was conducted to determine the relative influence of identified epistemic, technological, and operational uncertainty parameters. This revealed the strong influence of the fairing drag reduction estimate, the technological state-of-the art of major architecture components, and operational variables such as the storage tank discharge time on architecture performance. The results presented in this work highlight

1) the importance of designing flow-efficient active flow control systems, 2) the need to be able to better predict the mass flow requirements through computational analyses in early design phases, and 3) the importance of considering and trading off multiple system architectures. Avenues for future work include 1) extension of the analysis to include active flow control solutions that do not require pneumatic power (airflow), 2) extension to include smaller single-aisle aircraft and very large aircraft within the purview of the analysis, and 3) extension to account for more detailed spatial integration considerations and higher-order impacts such as on manufacturing, operation, and maintenance costs.

Appendix A: Mass Flow Distribution Logic

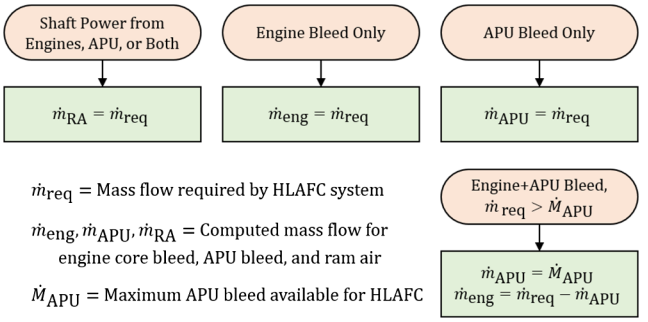

Fig. A1 Architectures using either only bleed or only shaft-power.

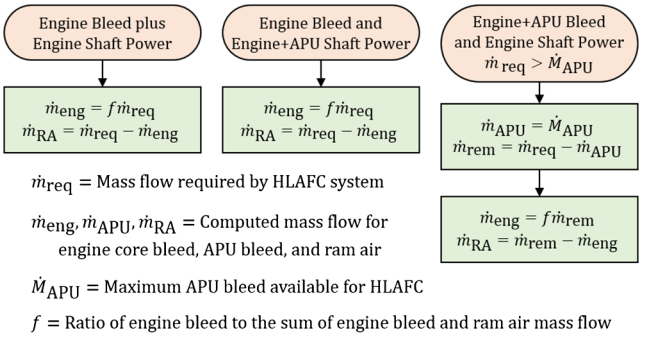

Fig. A2 Architectures where engines supply both bleed and shaft-power.

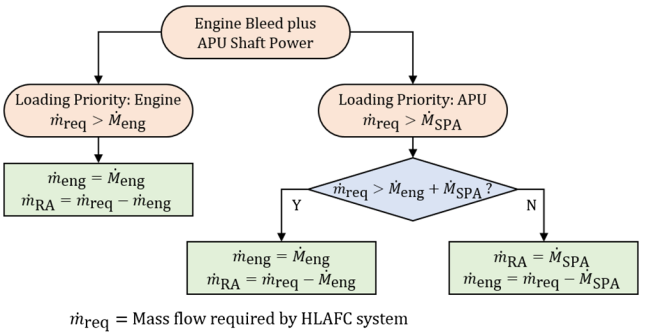

Fig. A3 Architectures where engines supply bleed and APU supplies shaft-power.

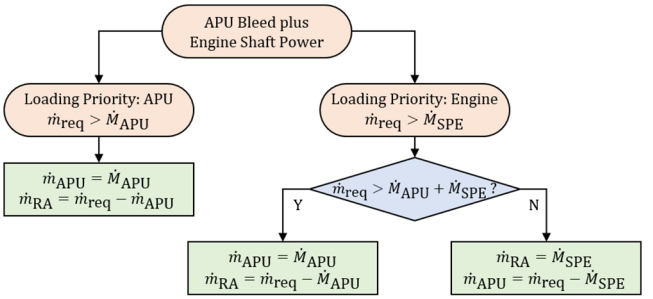

Fig. A4 Architectures where engines supply shaft-power and APU supplies bleed.

Appendix B: Nominal Values of Parameters

Table B1 Parameter summary for pneumatic ducting mass estimation (Sec. IV.D)

Parameter	Description	Value	Source/comments
p_{nom}	Nominal pressure	330 kPa	[31,32]
p_b	Burst pressure	$3P_{nom}$	14 code of federal regulations, Sec. 25.1438 [33]
T_{nom}	Nominal temperature	200°C	[31]
ρ_{duct}	Material density	4510 kg/m^3	Ti Gr.2/Gr.3 [29]
σ_{max}	Maximum permissible stress	49.5 MPa	Based on [29]
Y	Coefficient for nonferrous metals	0.4	[29]
Δp	Maximum permissible pressure loss	35 kPa	Assumed

Table B2 Summary of component efficiencies

Component	Symbol	Value	Source/comments
VF generator	η_{gen}	0.92	[34]
Power electronics	η_{pe}	0.97	[34]
Power networks	η_{ac}	0.95	Based on [35]
Compressor	η_{cmp}	0.85	[18]
Electric motor	η_{em}	0.90	[34]
Ram diffuser	η_{rd}	0.97	Assumed

Table B3 Summary of power-to-mass ratios

Component	Symbol	Value, kW/kg	Source/comments
VF generator	$(P/M)_{gen}$	2.76	[18]
Power electronics	$(P/M)_{pe}$	2	[18]
Motor	$(P/M)_{em}$	4	[18]
Compressor	$(P/M)_{cmp}$	2.5	[18]

Table B4 Parameter summary for storage tank (Sec. IV.E)

Parameter	Description	Value	Source/comments
D_{tank}	Tank diameter	5 ft	Assumed
L_{tank}	Tank length	13 ft	Assumed
t_{chg}	Charging time	600 s	Assumed
t_{dischg}	Discharging time	20 s	Assumed
h_{chg}	Charging altitude	10,000 ft	Assumed
V_{chg}	Charging airspeed	250 kt	Assumed
f_s	Factor of safety	1.4	Assumed
σ_y	Yield stress	2400 MPa	[30]
ρ_{mat}	Material density	8105 kg/m^3	[30]
$t_{w,min}$	Minimum wall thickness	1 mm	Assumed

Appendix C: Effect of System Mass Flow Requirement on Operating Empty Weight

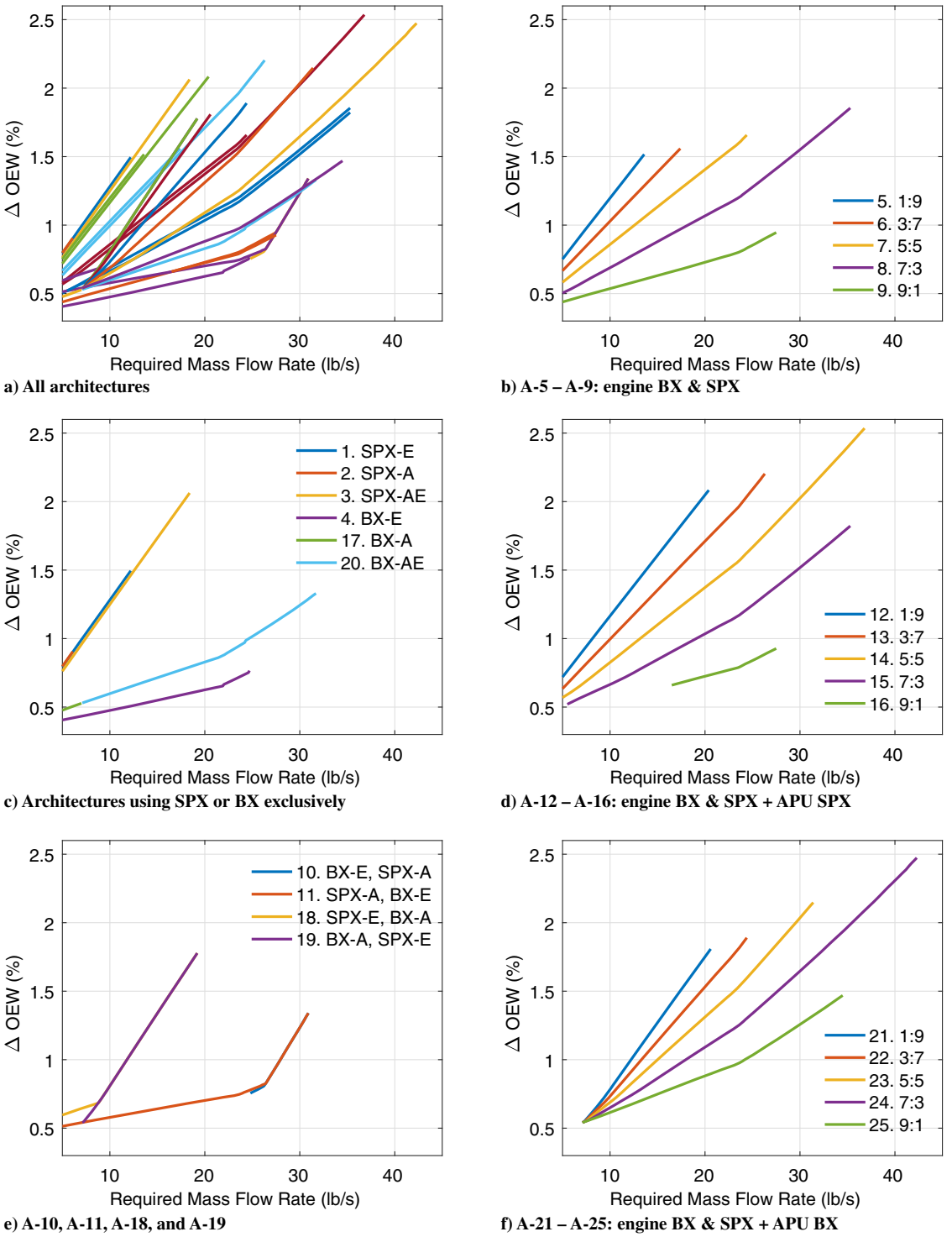

a) All architectures

b) A-5 – A-9: engine BX & SPX

c) Architectures using SPX or BX exclusively

d) A-12 – A-16: engine BX & SPX + APU SPX

e) A-10, A-11, A-18, and A-19

f) A-21 – A-25: engine BX & SPX + APU BX

Fig. C1 Impact of mass flow requirements on OEW of considered HLDAFC architectures.

References

[1] Kral, L. D., "Active Flow Control Technology," ASME Fluids Engineering Division, Technical Brief, 2000, http://citeseerx.ist.psu.edu/viewdoc/download?doi=10.1.1.515.1210&rep=rep1&type=pdf [retrieved 16 Oct. 2017].

[2] Collier, F., Thomas, R., Burley, C., Nickol, C., Lee, C.-M., and Tong, M., "Environmentally Responsible Aviation—Real Solutions for Environmental Challenges Facing Aviation," *27th Congress of International Council of the Aeronautical Sciences*, International Council of the Aeronautical Sciences Paper 2010-1.6.1, Nice, France, 2010.

[3] Schutte, J., Jimenez, H., and Mavris, D., "Technology Assessment of NASA Environmentally Responsible Aviation Advanced Vehicle Concepts," *49th AIAA Aerospace Sciences Meeting*, AIAA Paper 2011-0006, Jan. 2011.

[4] Andino, M. Y., Lin, J. C., Washburn, A. E., Whalen, E. A., Graff, E. C., and Wygnanski, I. J., "Flow Separation Control on a Full-Scale Vertical

Tail Model Using Sweeping Jet Actuators," *53rd AIAA Aerospace Sciences Meeting*, AIAA Paper 2015-0785, Jan. 2015.

[5] Hartwich, P. M., Dickey, E. D., Sclafani, A. J., Camacho, P., Gonzales, A. B., Lawson, E. L., Mairs, R. Y., and Shmilovich, A., "AFC-Enabled Simplified High-Lift System Integration Study," NASA CR-2014-218521, 2014.

[6] Jacobs, R., and Mavris, D. N., "System-Level Performance Impact of Active Flow Control Vertical Tails on a Commercial Transport Model Family," *14th AIAA Aviation Technology, Integration, and Operations Conference*, AIAA Paper 2014-3011, June 2014.

[7] Kuchan, A., "The Integration of Active Flow Control Devices into Composite Wing Flaps," M.S. Thesis, Georgia Inst. of Technology, Atlanta, GA, Aug. 2012, https://smartech.gatech.edu/handle/1853/44758 [retrieved 16 Oct. 2017].

[8] Lin, J. C., Andino, M. Y., Alexander, M. G., Whalen, E. A., Spoor, M. A., Tran, J. T., and Wygnanski, I. J., "An Overview of Active Flow Control Enhanced Vertical Tail Technology Development," *54th AIAA Aerospace Sciences Meeting*, AIAA Paper 2016-0056, Jan. 2016.

[9] Mooney, H. P., Brandt, J. B., Lacy, D. S., and Whalen, E. A., "AFC-Enabled Vertical Tail System Integration Study," NASA CR-2014-218168, 2014.

[10] Whalen, E. A., Lacy, D. S., Lin, J. C., Andino, M. Y., Washburn, A. E., Graff, E. C., and Wygnanski, I. J., "Performance Enhancement of a Full-Scale Vertical Tail Model Equipped with Active Flow Control," *53rd AIAA Aerospace Sciences Meeting*, AIAA Paper, 2015-0784, Jan. 2015.

[11] Whalen, E. A., "Flight Services and Aircraft Access: Active Flow Control Vertical Tail and Insect Accretion and Mitigation Flight Test," NASA CR-2016-219005, 2016.

[12] Bertels, F. G. A., van Dijk, R., Elmendorp, R., and Vos, R., "Impact of Pulsed Jet Actuators on Aircraft Mass and Fuel Consumption," *CEAS Aeronautical Journal*, Vol. 7, No. 4, Aug. 2016, pp. 535–549. doi:10.1007/s13272-016-0201-8

[13] Rudolph, P., "High Lift Systems on Subsonic Commercial Airliners," NASA CR 4746, Sept. 1996, https://ntrs.nasa.gov/archive/nasa/casi.ntrs.nasa.gov/19960052267.pdf [retrieved 16 Oct. 2017].

[14] Hartwich, P. M., Shmilovich, A., Lacy, D. S., Dickey, E. D., Scalafani, A., Sundaram, P., and Yadlin, Y., "Refined AFC-Enabled High-Lift System Integration Study," NASA CR-2016-219170, 2016.

[15] Hartwich, P. M., Camacho, P., El-Gohary, K., Gonzales, A. B., Lawson, E. L., and Shmilovich, A., "System-Level Trade Studies for Transonic Transports with Active Flow Control (AFC) Enhanced High-Lift Systems," *55th AIAA Aerospace Sciences Meeting*, AIAA Paper 2017-0321, Jan. 2017.

[16] DeSalvo, M., Gissen, A. N., Whalen, E. A., and Glezer, A., "High-Lift Performance Enhancement of a Simple Flap Using Aerodynamic Flow Control," *8th AIAA Flow Control Conference*, AIAA Paper 2016-3306, June 2016. doi:10.2514/6.2016-3306

[17] Sinnett, M., "Boeing 787 No-Bleed Systems: Saving Fuel and Enhancing Operational Efficiencies," *Boeing Aero Magazine*, No. 4, 2007, http://www.boeing.com/commercial/aeromagazine/articles/qtr_4_07/AERO_Q407_article2.pdf [retrieved 16 Oct. 2017].

[18] Chakraborty, I., "Subsystem Architecture Sizing and Analysis for Aircraft Conceptual Design," Ph.D. Thesis, Daniel F. Guggenheim School of Aerospace Engineering, Georgia Inst. of Technology, Atlanta, GA, Dec. 2015, https://smartech.gatech.edu/handle/1853/54427 [retrieved 16 Oct. 2017].

[19] McCullers, L., "Aircraft Configuration Optimization Including Optimized Flight Profiles," *Recent Experiences in Multidisciplinary Analysis and Optimization*, NASA CP-2327, 1984, pp. 395–412.

[20] Claus, R. W., Evans, A. L., and Follen, G. J., "Multidisciplinary Propulsion Simulation Using NPSS," *4th Symposium on Multidisciplinary Analysis and Optimization*, AIAA Paper 1992-4709, Sept. 1992.

[21] Chakraborty, I., and Mavris, D. N., "Integrated Assessment of Aircraft and Novel Subsystem Architectures in Early Design," *Journal of Aircraft*, Vol. 54, No. 4, July 2017, pp. 1268–1282. doi:10.2514/1.C033976

[22] Chakraborty, I., and Mavris, D. N., "Assessing Impact of Epistemic and Technological Uncertainty on Aircraft Subsystem Architectures," *Journal of Aircraft*, Vol. 54, No. 4, July 2017, pp. 1388–1406. doi:10.2514/1.C034007

[23] "Advisory Circular 25-20—Pressurization, Ventilation and Oxygen Systems Assessment for Subsonic Flight Including High Altitude Operation," Federal Aviation Administration, U.S. Dept. of Transportation, AC 25-20, Washington, D.C., Sept. 1996, https://www.faa.gov/documentLibrary/media/Advisory_Circular/AC25-20.pdf.

[24] Jones, R. I., "The More Electric Aircraft—Assessing the Benefits," *Proceedings of the Institution of Mechanical Engineers, Part G: Journal of Aerospace Engineering*, Vol. 216, No. 5, May 2002, pp. 259–269. doi:10.1243/095441002321028775

[25] Nelson, T., "787 Systems and Performance," Flight Operations Engineering, Boeing Commercial Airplanes, Boeing Commercial Airplanes, Seattle, WA, March 2009, http://myhres.com/Boeing-787-Systems-and-Performance.pdf [retrieved 16 Oct. 2017].

[26] Torenbeek, E., "Development and Application of a Comprehensive, Design-Sensitive Weight Prediction Method for Wing Structures of Transport Category Aircraft," Delft Univ. of Technology, Rept. LR-693, Delft, The Netherlands, Sept. 1992.

[27] Schoensleben, S., "Integrated Trailing Edge Flap Track Mechanism for Commercial Aircraft," M.S. Thesis, Swiss Federal Inst. of Technology Zurich, Zurich, 2006, http://e-collection.library.ethz.ch/eserv/eth:28634/eth-28634-01.pdf [retrieved 16 Oct. 2017].

[28] Parrilla, X., "Hybrid Environmental Control System Integrated Modeling Trade Study Analysis for Commercial Aviation," Ph.D. Thesis, University of Cincinnati, Cincinnati, OH, 2014, https://etd.ohiolink.edu/!etd.send_file?accession=ucin1396454368&disposition=inline [retrieved 16 Oct. 2017].

[29] Peacock, D., "Effective Design Using Titanium," *Proceedings of the International Conference on Titanium in Practical Applications*, Ginatta Tecnologie, Norwegian Association of Corrosion Engineers, Moncalieri, Italy, 1990, http://www.ginattatecnologie.it/Docs/Meeting6/VI%20Meeting%20-%2003.pdf. [retrieved 16 Oct. 2017].

[30] "18 Per Cent Nickel Maraging Steels—Engineering Properties," Publication No. 4419, Nickel Development Inst., Inco Europe Ltd., Rept. 4419, 1976, http://www1.diccism.unipi.it/Valentini_Renzo/slides%20lezione%20met.%20meccanica/18_NickelMaragingSteel_EngineeringProperties_4419_.pdf [retrieved 16 Oct. 2017].

[31] "Airbus A330 Flight Crew Operating Manual—Pneumatic," Airbus Industries, Toulouse, France, http://www.smartcockpit.com/aircraft-ressources/A330-Pneumatic.html [retrieved 04 Nov. 2015].

[32] "Airbus A319/A320/A321 Pneumatics," Airbus Industries, Toulouse, France, http://www.smartcockpit.com/aircraft-ressources/A319-320-321-Pneumatics.html [retrieved 4 Nov. 2015].

[33] "Federal Aviation Regulations (FAR) Part 25—Airworthiness Standards: Transport Category Airplanes," Federal Aviation Administration, U.S. Dept. of Transportation, Washington, D.C., https://www.ecfr.gov/cgi-bin/text-idx?node=14:1.0.1.3.11 [retrieved 16 Oct. 2017].

[34] Whyatt, G., and Chick, L., "Electrical Generation for More-Electric Aircraft Using Solid Oxide Fuel Cells," Pacific Northwest National Lab., Rept. PNNL-21382, Richland, WA, April 2012.

[35] "Advisory Circular AC 43.13-1B—Acceptable Methods, Techniques, and Practices—Aircraft Inspection and Repair," Federal Aviation Administration, U.S. Dept. of Transportation, Rept. AC 43.13-1B, Sept. 1998, http://www.faa.gov/documentLibrary/media/Advisory_Circular/AC_43.13-1B_w-chg1.pdf [retrieved 16 Oct. 2017].